

Molecular Vibration and Charge Transport in Crystalline Oligoacenes and Derivatives: Raman and DFT Combined Study

by

Zhongqiao Ren

A dissertation submitted to the faculty of the University of North Carolina at Chapel Hill in partial fulfillment of the requirements for the degree of Doctor of Philosophy in the Department of Physics and Astronomy.

Chapel Hill

2010

Approved by:

Dr. Laurie McNeil, Advisor
Dr. Charles Evans, Reader
Dr. Rene Lopez, Reader
Dr. Jianping Lu, Reader
Dr. Lu-Chang Qin, Reader

©2010
Zhongqiao Ren
ALL RIGHTS RESERVED

ABSTRACT

ZHONGQIAO REN: Molecular Vibration and Charge Transport in Crystalline Oligoacenes and Derivatives: Raman and DFT Combined Study
(Under the Direction of Dr. Laurie McNeil)

All-organic devices have drawn a lot of interest over the past decades. Compared to liquid crystal display technology, organic transistors and discrete LED displays hold the potential for devices with improved characteristics, including lower power requirements, better resolution, more mechanical flexibility, and lower production costs. To find new materials for better device performance, it is necessary to understand the connection between the structural and electronic properties of molecules. The establishment of these connections will make it possible to tailor molecules for desired performance in devices.

Among the organic materials, oligoacenes and their derivatives have an important position in fundamental physics research because the molecules are relatively small and simple, which facilitates understanding of the relationships among molecular structures, optical properties, and transport properties in organics. In this work, I focus on the molecular vibration and charge transport in three oligoacene and two oligoacene derivative single crystals: anthracene, tetracene, pentacene, 9,10-diphenylanthracene (DPA), and especially 5,6,11,12-tetraphenyltetracene (rubrene).

By comparing the experimental Raman spectra with the Density-Functional-Theory calculation based on one isolated molecule, I am able to distinguish the intermolecular vibrations from the intramolecular vibrations in crystalline anthracene, tetracene, pentacene, and DPA. Parallel study among the oligoacenes reveals decreasing strength of intermolecular vibrations as the number of benzene ring increases. However, the intermolecular coupling is even weaker in

DPA because the side phenyl groups prevent close packing, therefore several intramolecular vibrational modes predicted by the calculation can be observed in the low-frequency Raman spectrum.

I report temperature-dependent Raman spectra of rubrene from 30 to 300 K. The linewidths of certain low-frequency peaks increase significantly with temperature, especially in the range 150–200 K. These peaks correspond to the vibrations of the phenyl side groups of the rubrene molecules, and their couplings to intermolecular vibrational modes. I propose a model in which the strong increase in mobility observed with increasing temperature between 30 and 150 K results from disorder as the phenyl groups exchange sides of the backbone plane and break the symmetry, and discuss on how this model explains previous experimental observations of structural and calorimetric changes near 150 K. Lastly I discuss possible temperature-dependent properties of rubrene, and the potential application of the rubrene molecule in single-molecule devices design.

ACKNOWLEDGMENTS

Pursuing the Ph.D. degree in a foreign country is not easy, but fortunately I have received a lot of help and encouragement from different people. First of all, I would like to express my cordial gratitude to Dr. Laurie McNeil, under whose guidance I finished my Ph.D. study. Being the department chair during the past years, Laurie took heavy administration workload, however she still managed to sit down with me every week and listen to my research progresses patiently. She always encouraged me to solve problems independently, and meanwhile responded to my requests quickly. I have benefited a lot from her enthusiasm in science and preciseness in research. Dr. Shubin Liu of high-performance computing group at UNC helped me a lot in the molecular vibration simulation, DFT calculation, as well as the results interpretation, and Dr. Christian Kloc at Nanyang Technological University supplied all of my samples, —the project can't be successful without their generous help. I am also thankful to other professors in the department for their inspiring discussion, i.e., Drs. John Hernandez, Lu-Chang Qin, Jianping Lu, Rene Lopez, Charles Evans, and Alfred Kleinhammes.

Drs. Jennifer Weinberg-Wolf, Eric Harley, and Kristopher McGuire are all great lab mates, from whom I have received patient and systematic training on equipments operation and research methodology. I will never forget the days that I spent with my classmates Miguel Perez, Adrian Serohijos, and Richard Crooks when we were preparing for the qualifying exams together, —discussing physics problems with them was so pleasing and instructive. Thanks to other friends in the department, who have made my life at UNC so cheerful and colorful.

Especially I want to thank Haijing Wang, a curious and diligent physicist, who is always willing to listen to me and help solve problems in a field totally out of his own research. I believe it is these selfless dedications that make the whole community such a friendly one.

My special gratitude goes to Vivien Lo, who has been standing by me since our first meeting and keeps encouraging me during the tough time. I can't imagine how I could survive the long days doing experiments in the lab without her encouragements. Last but definitely not least, I must thank my dearest parents for their endless love and support. They have provided me with all the best that they are able to give, however I have little to return. To them I dedicate this dissertation.

Zhongqiao Ren

July 15, 2010

Dedicated to:

My dearest parents, Qingyou Ren and Ping Wang

CONTENTS

	Page
LIST OF TABLES	iii
LIST OF FIGURES	iv
Chapter	
I. Introduction	8
1.1 Overview	8
1.2 Molecular Crystals	10
1.2.1 Oligoacenes: Anthracene, Tetracene and Petancene . . .	10
1.2.2 Oligoacene Derivatives: DPA and Rubrene	13
II. Experiment and Simulation	18
2.1 Crystal Growth	18
2.2 Raman Spectroscopy	19
2.2.1 Classical Theory	21
2.2.2 Quantum Theory	23
2.2.3 Temperature Effects	26
2.3 Experimental Setup	31
2.4 Calculations Based on Density Functional Theory	36
III. Molecular Vibration in Oligoacenes and Oligoacene Derivatives . . .	39
3.1 The Crystals	40
3.2 Raman Spectra	44
3.3 Conclusion	47
IV. Molecular Vibration in Rubrene: Raman Study and A New Model .	48
4.1 The Rubrene Crystal	48

4.2	Raman Spectra	53
4.2.1	Experimental Conditions	53
4.2.2	Temperature Dependent Raman Results	54
4.3	A New Molecular Motion Model	61
4.3.1	Intuitive Explanation	64
4.3.2	Classical Theory	64
4.3.3	Quantum Mechanical Theory	66
4.4	Simulations	68
4.5	Conclusion	71
V.	Impacts of Our Molecular Motion Model	72
5.1	Mobility	72
5.2	Thermal, Structural and Other Properties	75
5.3	Application in Single-Molecule Devices	78
5.4	Conclusion	80
VI.	Conclusions	81
VII.	REFERENCES	84

LIST OF TABLES

3.1	Atomic Positions in Anthracene	41
3.2	Atomic Positions in Tetracene	42
3.3	Atomic Positions in Pentacene	42
3.4	Atomic Positions in Diphenylanthracene	43
4.1	Atomic Positions in Rubrene	50
4.2	Phenyl Group Torsion Angle ϕ as a Function of Temperature in Rubrene Molecule	53
4.3	Allowed Raman Modes for C_{2h} Point Group (Before Flipping) with Backscattering Geometry	67
4.4	Allowed Raman Modes for D_2 Point Group (After Flipping) with Backscattering Geometry	67

LIST OF FIGURES

1.1	Oligoacene Molecules	11
1.2	9,10-Diphenylanthracene (DPA) Molecule	13
1.3	5,6,11,12-Tetraphenyl Tetracene (Rubrene) Molecule	14
1.4	Experimental Hole Mobility as a Function of Temperature in Rubrene Single Crystals	16
2.1	Light Scattering Schematic	20
2.2	Feynman Diagrams for Stokes Raman Scattering	24
2.3	Temperature Dependence of Raman Frequency and Line Width in Si, Ge, and α -Sn	32
2.4	Raman Spectrometer Schematic	33
3.1	Anthracene ($C_{14}H_{10}$) Molecule	41
3.2	Tetracene ($C_{18}H_{12}$) Molecule	42
3.3	Pentacene ($C_{22}H_{14}$) Molecule	42
3.4	Diphenylanthracene ($C_{26}H_{18}$) Molecule	43
3.5	Room Temperature Raman Spectrum of Anthracene, Tetracene, Pentacene, and Diphenylanthracene Single Crystals	45
3.6	Room Temperature Low-Energy Experimental Data and The- oretical Predictions for Anthracene, Tetracene, Pentacene, and DPA Single Crystals	46
4.1	Rubrene ($C_{42}H_{28}$) Molecule	49
4.2	Three Views of the Packing in the Rubrene Single Crystal	51
4.3	Packing of Two Nearest-Neighbor Molecules in the Rubrene Crystal	52
4.4	Molecular Displacement d as a Function of Temperature in Rubrene	53
4.5	Room Temperature Raman Spectrum of Rubrene Single Crystals	55
4.6	Low Temperature Raman Spectrum of Rubrene Single Crystals	56
4.7	Comparison of Rubrene Low-Frequency Raman Peaks at Room Temperature (300 K) and Low Temperature (30 K)	57
4.8	Evolution of Low-Frequency Raman Peak Positions with Tem- perature in Rubrene	58

4.9	Evolution of Low-Frequency Raman Peak Line Widths with Temperature in Rubrene	60
4.10	Possible Phenyl Side Group Positions in Rubrene with Different Energies	63
4.11	Evolution of Energy Differences Between Different Phenyl Group Positions with Temperature	69
5.1	Differential Scanning Calorimetry of Crushed Rubrene Single Crystals	76
5.2	Molecular and Lattice Structure for 5,12-BTBR	78

Chapter 1

Introduction

1.1 Overview

Over the past decades, the optical properties of organic molecular crystals have drawn a lot of interest. Introduction and review of the optically-active materials can be found in many publications, such as reference [1]. Especially since the first organic light-emitting device (OLED) was successfully fabricated using tris-8-hydroxyquinoline aluminum (Alq_3) in 1987 [2], interest in the applications of thin films of these organic molecular materials has grown. The first organic field-effect transistor (OFET) based on sexithiophene came out in 1996 [3], and it opened the door to a brand-new commercial product: all-organic devices consisting of OLEDs and OFETs. Compared to liquid crystal display (LCD) technology, organic transistors and discrete LED displays hold the potential for devices with improved characteristics, including lower power requirements, higher resolution, more mechanical flexibility, and lower production costs. Plenty of reviews of recent progress in thin film technology using organic materials can be found in the literature [4–6].

Among organic materials, polycyclic aromatic compounds such as the π -conjugated oligoacenes and their derivatives are of particular interest. Their molecules are relatively small and simple, and the highest occupied molecular

orbital (HOMO)-lowest unoccupied molecular orbital (LUMO) separations are typically in the visible range, which makes them appealing for display applications. In the crystalline state these materials still have optical transitions in the visual range, which is crucial for optical device applications. Many different molecules have been studied and numerous devices have been fabricated from these molecular crystals [7, 8], including FETs [9–15], LEDs [2, 16–19], photovoltaic cells [20, 21], a chemical UV actinometer [22], and chemical sensors [23, 24]. It is therefore important to have an understanding of the relationships among crystal structure, optical properties, and transport properties of a material to facilitate the device applications. Once these connections are well understood, it will be possible to tailor molecules for desired performance in devices.

Many of the important characteristics of these materials for device manufacturing depend on the microstructure of the thin films and single crystals used. Furthermore, the rapid progress in single-molecule device fabrication recently [25–30] demands a better understanding of the molecular vibration and transport properties. High-quality single crystals that are relatively free of defects and impurities provide a perfect platform for studies of the “intrinsic” qualities of the thin films and molecules. On the other hand, optical spectroscopy is an excellent method to probe the different intrinsic properties since it is non-destructive. Information about the molecular vibrations at different temperatures, also derived through optical studies, could have an impact on single-molecule device design. This dissertation covers the molecular vibration properties of four different molecules and single crystals: anthracene, tetracene, pentacene, 9,10-diphenylanthracene (DPA), and focuses on the optical characterization of another one: 5,6,11,12-tetraphenyl tetracene (rubrene). This primary analysis method used here is Raman Spectroscopy, as well as computer calculations from GAUSSIAN 03, which are used to compare with and support the experimental data.

1.2 Molecular Crystals

The bonding in molecular crystals comprises two force regimes: strong covalent bonds within molecules and weak van der Waals forces between molecules. Because of the weak forces between molecules, such materials maintain many of the same characteristics as in the individual molecular components in the solid state, and hence are designated as molecular crystals. The weakness of the van der Waals bonds between molecules means that in the solid state, molecular crystal systems have very low lattice energy. As expected, this low lattice energy causes molecular crystals generally to have low melting and sublimation temperatures, low mechanical strength, and high compressibility. The packing of somewhat large molecules into the solid state leads to molecular crystals that tend to have low symmetry; therefore, anisotropy is not uncommon in many different crystal properties, e.g., optical, electronic, magnetic, and mechanical ones. Also, since the forces between molecules are very weak, it is possible to have several different lattice arrangements that all have similar ground state energies; thus polymorphism is very common.

Although the vibrational and electronic structures of the individual molecules are similar in the crystal state of molecular crystals, crystal field effects do exist. Most notable is the Davydov splitting of bands in both the electronic and vibrational spectra. The presence of more than one molecule in the unit cell causes Davydov, or factor group, splitting. The multiple molecules in the unit cell will interact, thereby lifting degeneracies in energy of the original molecular spectrum.

1.2.1 Oligoacenes: Anthracene, Tetracene and Pentacene

Oligoacenes are ladder-like hydrocarbon molecules with multiple benzene rings fused together. Researchers have focused on the three-ring (anthracene), four-ring (tetracene, also known as naphthacene) and five-ring (pentacene) com-

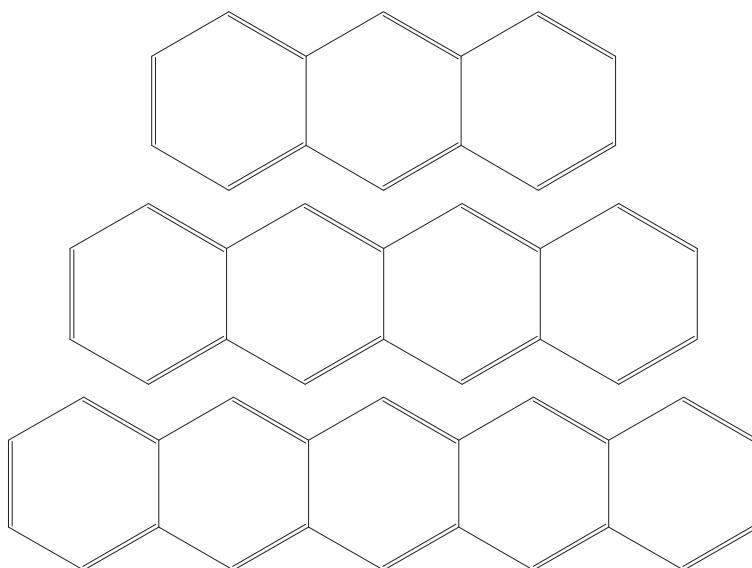


Figure 1.1: Molecular structures of oligoacenes. In order of increasing number of rings: anthracene, tetracene (also known as naphthacene) and pentacene.

pounds depicted in figure 1.1. All of the molecules have D_{2h} point group symmetry, and their crystals have C_i point group symmetry. The sp^2 hybridization of the valence carbon atoms causes the planarity of the molecules. Because of the difficulty of growing high-quality single crystals and the confusing existence of multiple polymorphs, systematic studies of the optical and vibrational properties have only recently been possible. The presence of defects and grain boundaries strongly influences the measured optical and transport properties of polycrystalline films of these materials.

One of the smaller molecules, anthracene, is a chain of three fused benzene rings. The Raman signature of anthracene studied in single crystals [31, 32], thin films [33], powder [34], and solutions [35], at multiple temperatures [36, 37] and various pressures [38, 39], and by theoretical calculations [40, 41] gives a complete picture of the vibrational structure of the molecule, although investigations on high-purity samples are still lacking. Using Brillouin scattering [42] and inelastic neutron scattering (INS) [43], researchers have been able to measure the elastic constants of the single crystal. Photoconduction experiments

on anthracene [44–46] yield values for the band gap between 3 and 4 eV. Scientists have also conducted experiments to measure the luminescence of single crystals [46,47] at multiple temperatures [48] and at different pressures [49]. The spectra indicate a very strong coupling of excitons to intramolecular vibrations. Data from reflectivity studies of sublimed films [50] indicate that the \vec{a} and \vec{b} axes of the crystallites tend to lie in the plane of the substrate, a structural geometry similar to that found in other oligoacene thin films and crystallites. The full crystallographic information for the crystal at multiple temperatures is also available from X-ray diffraction studies [51]. A recent high-pressure Raman study of the material observed an abrupt line width broadening at 2.4 GPa [52], possibly due to a previously-suggested second-order phase transition at this pressure [53].

Tetracene has a measured band gap of 3–3.5 eV [54,55]. As with anthracene, researchers have measured the photoluminescence spectrum at a variety of temperatures. The spectrum reveals a variety of free and trapped excitons, the energies of which depend on the structural characteristics and possible defects of the crystal [56]. The crystal field effects (Davidov splitting) are very similar for anthracene and tetracene [57]. Researchers have measured the exciton-phonon coupling constant g to be 0.77 [58,59], where $g = E_{LR}/B$ and E_{LR} is the lattice relaxation energy while B is the exciton band halfwidth. For $g < 1$, excitons are not self-trapped. Tetracene has a very high hole mobility; values between $0.8 \text{ cm}^2/\text{Vs}$ [54] and $1.3 \text{ cm}^2/\text{Vs}$ [60] in high-quality crystals approach and even exceed the mobility of amorphous silicon. The vibrational modes for the gas phase of both tetracene and pentacene molecules from experiments [61] and theoretical calculations [62] are available in the literature. Early Raman measurements of tetracene crystals can be found in the literature [63–66], however the measurements have been of lower quality crystals or on older instruments incapable of high resolution and high signal-to-noise ratio. A recent comprehensive study that collected data about the vibrational structure as a function of temperature and pressure has improved the general understanding of the struc-

ture of this molecule [67]. Raman measurements also confirm the coexistence and inter-conversion of two polymorphs in the crystal, which was observed in an X-ray diffraction study [68] and in the temperature-dependent mobility measurements [5] of the tetracene crystal.

Pentacene has a measured band gap of approximately 1.8 eV [69, 70]. Researchers have measured the single crystal mobility of pentacene to be $1.4 \text{ cm}^2/\text{Vs}$ [60] while scientists predict a value as high as $\sim 75 \text{ cm}^2/\text{Vs}$ for very pure single crystals [71]. As with tetracene, however, the transport properties vary greatly depending on materials preparation and the structural defects in the resulting crystals and thin films [72, 73]. Measurements exist for reflection spectra [74], photoluminescence spectra [75] and Raman spectra [63, 76]. Different molecule packings exist in pentacene thin films, bulks, and single crystals [77], and Raman spectra have observed at least two polymorphs in the single crystal [78]. Crystallographic data are available for some of these polymorphs [79].

1.2.2 Oligoacene Derivatives: DPA and Rubrene

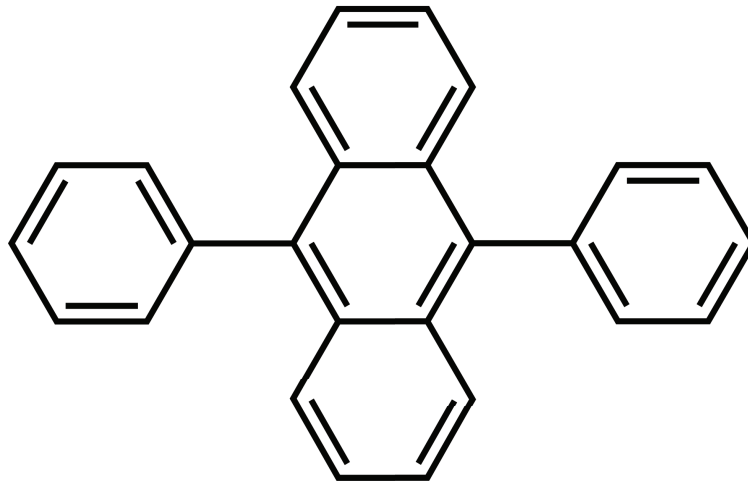


Figure 1.2: Molecular structures of DPA, an anthracene derivative.

9,10-Diphenyl anthracene, commonly known as DPA, has a slightly more complicated molecular structure. DPA is a small aromatic hydrocarbon consisting

of a backbone of three fused benzene rings (anthracene) with two substituted phenyl groups (one on each side attached to the central ring) as shown in figure 1.2. DPA has an almost 100% photoluminescent yield, and has been used as one of the standard materials for quantum yield comparison [80]. Early publications have reported its absorption spectrum [81], and resonance Raman spectra of its cation and anion radicals [82]. Its mobility measured at room temperature reaches $13\text{ cm}^2/\text{Vs}$ for electrons and $3.7\text{ cm}^2/\text{Vs}$ for holes, and the hole mobility follows a bandlike transport at high temperatures (200–400 K) and a saturation behavior in the low-temperature regime [83]. With study on the actual vibrational structure still lacking, there seems to be only one polymorph in this material, although recent measurements have suggested that DPA crystallized from solution may have a different lattice structure from vapor-grown crystals.

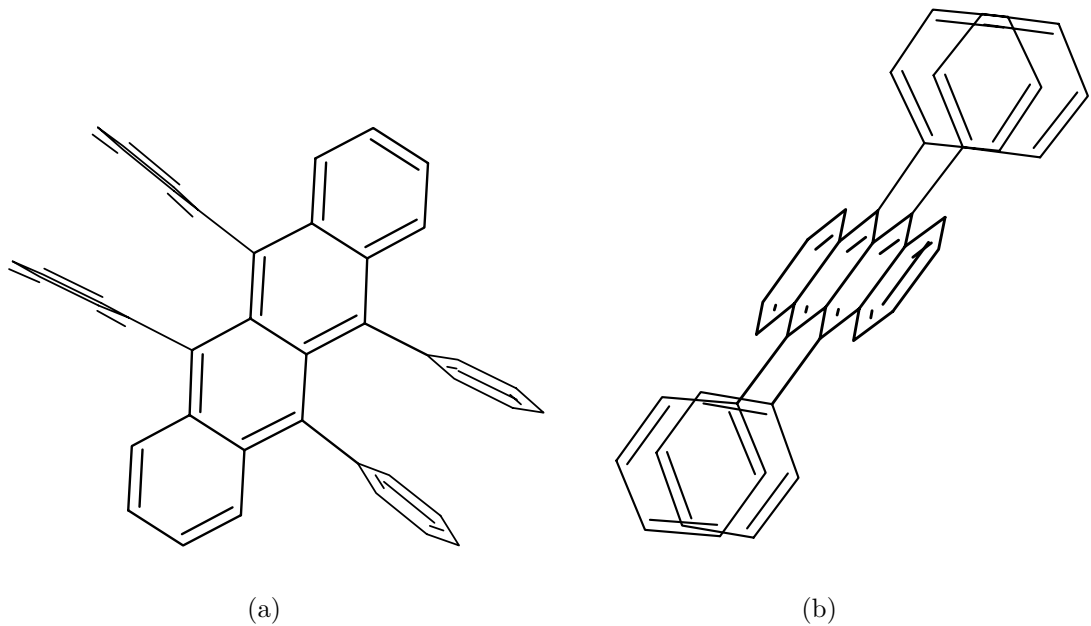


Figure 1.3: Molecular structures of rubrene, a tetracene derivative.

Even more complicated is the substituted oligoacene 5,6,11,12-tetraphenyl tetracene, commonly known as rubrene. Rubrene is a relatively small aromatic hydrocarbon consisting of a backbone of four fused benzene rings (tetracene)

with four substituted phenyl groups (two on each internal ring) as shown in figure 1.3. Steric hindrance dictates that the substituted phenyl groups rotate out of the plane of the tetracene backbone. The measured HOMO-LUMO gap of the molecule is approximately 2.2 eV [84,85]. Rubrene crystallizes in an orthorhombic structure [86, 87] with D_{2h}^{18} point group symmetry (while the molecule has C_{2h} point group symmetry), and has four molecules in the unit cell. The crystal also has a relatively high melting point (~ 590 K).

Rubrene has an almost 100% photoluminescent yield [88], and has been used in devices such as chemical sensors [89] and actinometers [22] as well as OLEDs [90, 91] and OFETs [5, 92]. Researchers have found the value of the hole mobility in rubrene single crystals in an FET structure with free-space gate dielectrics to be as high as $30 \text{ cm}^2/\text{Vs}$ and $20 \text{ cm}^2/\text{Vs}$ at low and room temperatures, respectively [92, 93]; the maximum mobility of carriers that penetrate deeper into the crystal reaches even $40 \text{ cm}^2/\text{Vs}$ at room temperature [94]. With other gate materials, e.g., ionic-liquid electrolytes, the mobility reaches up to $9.5 \text{ cm}^2/\text{Vs}$ [95], and measurements of Hall mobility yield nearly $10 \text{ cm}^2/\text{Vs}$ [96]. Although values vary with different configurations and along different axes, they are much higher than those of other organics that share similar molecular structures, such as tetracene ($1 \text{ cm}^2/\text{Vs}$) [5], and even that of amorphous hydrogenated silicon. Different groups report different results for the absolute value of the mobility at various temperatures, but in all measurements the mobility increases rapidly from low temperature to $\sim 150\text{--}175$ K, above which it decreases gradually as the temperature increases further [5, 92]. Figure shows this abnormal temperature dependence of mobility in rubrene. As a comparison, in pentacene the carrier mobility decreases gradually from low to room temperature [97, 98], which is consistent with a band model for charge transport. In tetracene the carrier mobility increases rapidly from low temperature to ~ 180 K, and then falls gradually up to room temperature [5]. As mentioned above, this behavior is ascribed to a phase transition observed near the temperature at which the mobility

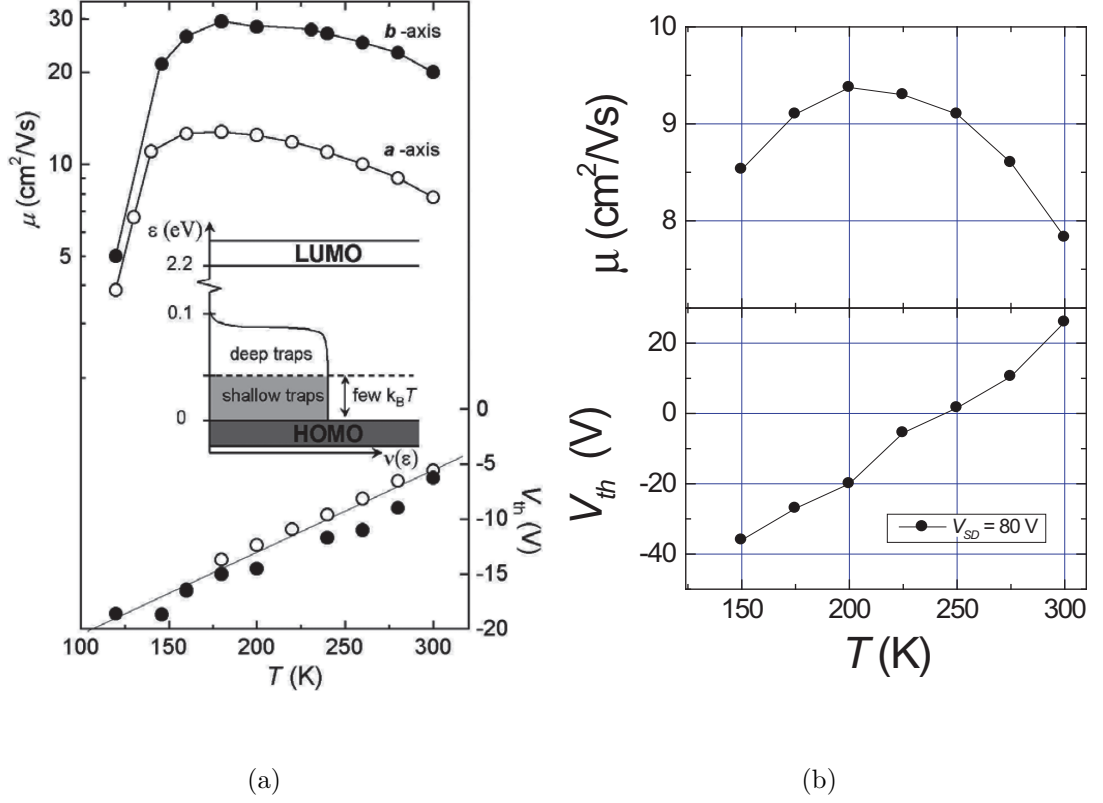


Figure 1.4: Experimental hole mobility as a function of temperature in rubrene single crystals measured by different research groups. (a) Graph is duplicated from reference [92]; (b) graph is duplicated from reference [5].

has its maximum [68]. However, there has been no X-ray evidence suggesting such a phase transition in rubrene over the 100–300 K temperature range [99], and room temperature polarized Raman spectra on various surfaces of the crystal observed no multi-phase coexistence [100]. Some claim that the mobility drop in the crystal below 140 K could be caused by trapping of carriers by shallow traps [5, 92], and another possible explanation proposed by Li *et al.* suggests that the enhancement of the effective mass of quasiparticles in molecular orbital bands may be responsible ($\mu = e\tau/m^*$) [101].

Other studies on rubrene include measurements of the absorption spectrum in the visible range for evaporated thin films [84, 102, 103], as well as the photoluminescence spectrum [88, 104, 105]. Older publications report a few Raman spectra

for unpurified thin films [63,106–108], however none of them focus on the actual vibrational structure of the material. Two recent articles have rectified this omission [100,109]. Investigators have also employed nonlinear optical spectroscopies to examine the electronic relaxation dynamics of rubrene and tetracene [110].

Chapter 2

Experiment and Simulation

Raman spectroscopy is a non-contact, non-destructive technique to study vibrational structures of crystals; more importantly, it is sensitive to the vibrational symmetry change with variation of the external conditions (such as temperature, pressure, and laser polarization), and is thus an excellent method with which to investigate the molecular structures of materials. Density Functional Theory (DFT) calculations at the molecule level provide supplemental information about the materials' electronic and vibrational properties. By combining temperature-dependent Raman scattering experiments and parallel simulations, I was able to study the properties of oligoacenes and their derivatives.

2.1 Crystal Growth

The samples used in this research were grown using the method of horizontal physical vapor transport in a flow of argon gas, starting with materials acquired from Aldrich. This part of work was done by Christian Kloc, of Bell Laboratories, Lucent Technologies (now at Nanyang Technological University, Singapore). More details about this growth process can be found in published work [111,112]. To grow thick bulk crystallites more suitable for this study, Dr. Kloc used some previously-sublimed rubrene crystals for a subsequent vacuum-sealed ampoule growth.

Although this method generates high-purity crystals, oxidation is very likely if the samples are exposed to the air. There have been many studies on impurities and their effects in organic semiconductors, and it has been pointed out that the highly-oxidized crystals may have dramatically different properties from pure ones. Therefore it is wise to distinguish the “intrinsic” properties from the ones induced by external conditions.

2.2 Raman Spectroscopy

Raman spectroscopy is based on the inelastic scattering of light. It is a non-destructive, non-invasive probe of the vibrational structure and phonon modes of a crystal. Chandrasekhara Venkata Raman received the 1930 Nobel Prize in physics for measuring and understanding this inelastic scattering effect (the phenomenon has been named after him). The basic experiment requires a monochromatic incident light source (usually a laser for its coherence and intensity), a means to separate the energies of the collected light (a spectrometer or spectrograph) and a detector (initially photographic paper, now photomultiplier tubes (PMTs) and charge-coupled devices (CCDs)).

Consider the example of a material irradiated by a high-intensity monochromatic light source. The molecules in the material will scatter this light, which one can collect for analysis. The majority of the scattering will be elastic, meaning that the scattered wavelength is equal to the incident wavelength. A very small proportion of the incident photons (one in 10^6), however, will undergo energy loss or gain, and the final state of the system will be different from the initial state. Figure 2.1 shows possible interactions between an incident photon and a crystalline medium, including different cases in Raman scattering described above as well as another process called photoluminescence (PL): the elastic process is called Rayleigh scattering and is the second process from the left in the schematic of the figure; the one in which the outgoing photon has more energy

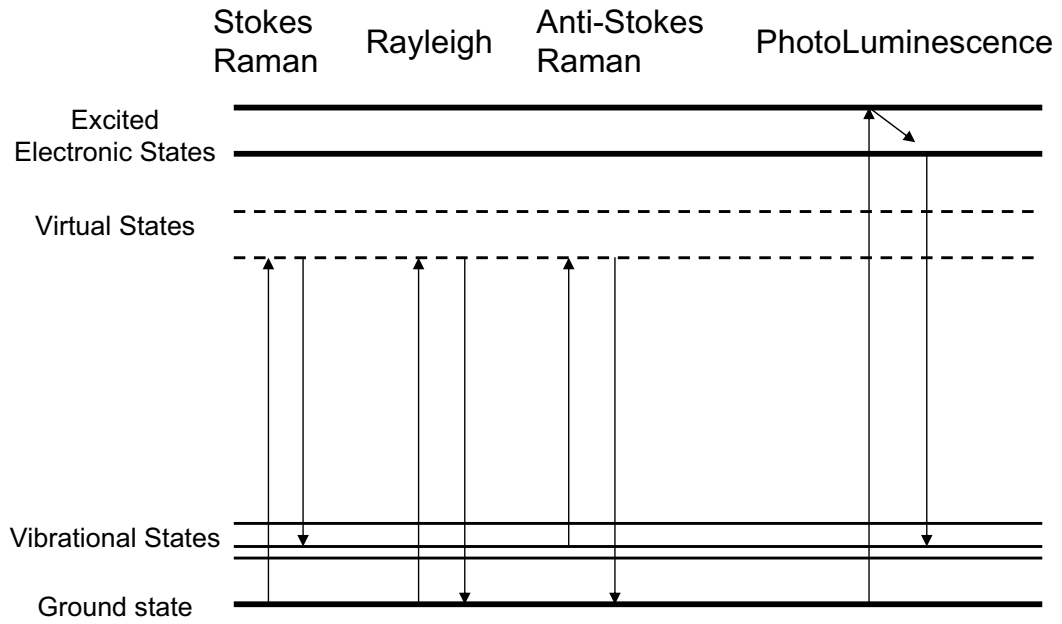


Figure 2.1: Possible interactions between an incident photon and a crystalline medium. Rayleigh scattering is an elastic process, while the Stokes and anti-Stokes interactions pictured are the inelastic Raman scattering processes. The PL process involves direct emission of light and real excitations of electrons.

than the incident photon is called anti-Stokes scattering (the third from the left), and the one where the outgoing photon has less energy is called Stokes scattering (the first from the left). The two latter processes, i.e., Stokes and anti-Stokes scattering, are called Raman scattering in general. As a comparison, the PL process involves real rather than virtual excitations of electrons, in which excited electrons fall back to lower states through radiative recombination pathways and emit photons directly.

The exact energy shift between the incident and the scattered light will depend on the type and strength of the bonds in the material which determine the phonon energies, and this is why Raman spectrum of a particular material can be considered the vibrational fingerprint for the system, and the technique has been widely used to study polymorphism, electron-phonon coupling, and other related topics.

Magnetic excitations and electronic excitations in crystals, despite their smaller light-scattering cross sections, produce Raman scattering as well [113–116]. Therefore light scattering has also been one of the standard methods for determining the frequencies and other properties of magnetic and electronic excitations. Another inelastic light scattering process with quasiparticles is Brillouin scattering, which is distinguished from Raman scattering in that it involves acoustic phonons rather than optical ones, and has been usually used to measure materials' larger-scale properties, such as the elastic behavior. On the other hand PL spectra provide information about recombination pathways between ground and excited states, thus have been widely used to study the band structures of materials. In the following sections I will discuss macroscopic and microscopic theories only of vibrational excitations Raman scattering; more information about magnetic and electronic Raman scattering, Brillouin scattering, and PL spectroscopy, as well as their applications can be found elsewhere [117–119].

2.2.1 Classical Theory

Although Raman scattering is a quantum-mechanical interaction, it can be described utilizing the classical plane-wave polarization theory. The incident monochromatic light source is a sinusoidal electro-magnetic plane wave:

$$\vec{E}(\vec{r}, t) = \vec{E}_i(\vec{k}_i, \omega_i) \cos(\vec{k}_i \cdot \vec{r} - \omega_i t) \quad (2.1)$$

where ω is the frequency and \vec{k} is the wavevector of the incident radiation. This electric field will induce a sinusoidal polarization within the medium equal to:

$$\vec{P}(\vec{r}, t) = \chi(\vec{k}_i, \omega_i) \vec{E}_i(\vec{k}_i, \omega_i) \cos(\vec{k}_i \cdot \vec{r} - \omega_i t) \quad (2.2)$$

where $\chi(\vec{k}_i, \omega_i)$ is the susceptibility of the medium. The polarization has the same frequency and wavevector as the incident plane wave. One can expand $\chi(\vec{k}_i, \omega_i)$

as a Taylor series in the normal modes of vibration of the system $\vec{Q}(\vec{r}, t)$. Here, $\vec{Q}(\vec{r}, t)$ is defined to be:

$$\vec{Q}(\vec{r}, t) = \vec{Q}(\vec{q}, \omega_0) \cos(\vec{q} \cdot \vec{r} - \omega_0 t) \quad (2.3)$$

where \vec{q} and ω_0 are the wavevector and frequency of the normal mode. Expanding the susceptibility in terms of equation 2.3 yields

$$\begin{aligned} \chi(\vec{k}_i, \omega, \vec{Q}) &= \sum_{n=0}^{\infty} \left[\frac{1}{n!} \left(\frac{\partial^n \chi}{\partial \vec{Q}^n} \right)_0 \vec{Q}^n(\vec{r}, t) \right] \\ &= \chi_0(\vec{k}_i, \omega_i) + \left(\frac{\partial \chi}{\partial \vec{Q}} \right)_0 \vec{Q}(\vec{r}, t) + \dots \end{aligned} \quad (2.4)$$

Here χ_0 is the electric susceptibility in the absence of fluctuations and the first-order differential of χ is an oscillatory susceptibility induced by normal modes in the medium. For this classical representation, one needs to expand the susceptibility only to first order in $\vec{Q}(\vec{r}, t)$. Substituting equation (2.4) into equation (2.2) yields the induced polarization:

$$\vec{P}(\vec{r}, t, \vec{Q}) = \vec{P}_0(\vec{r}, t) + \vec{P}_{ind}(\vec{r}, t, \vec{Q}) \quad (2.5)$$

where

$$\vec{P}_0(\vec{r}, t) = \chi_0(\vec{k}_i, \omega_i) \vec{E}_i(\vec{k}_i, \omega_i) \cos(\vec{k}_i \cdot \vec{r} - \omega_i t)$$

and

$$\begin{aligned} \vec{P}_{ind}(\vec{r}, t, \vec{Q}) &= \left(\frac{\partial \chi}{\partial \vec{Q}} \right)_0 \vec{Q}(\vec{r}, t) \vec{E}_i(\vec{k}_i, \omega_i) \cos(\vec{k}_i \cdot \vec{r} - \omega_i t) \\ &= \left(\frac{\partial \chi}{\partial \vec{Q}} \right)_0 \vec{Q}(\vec{q}, \omega_0) \cos(\vec{q} \cdot \vec{r} - \omega_0 t) \vec{E}_i(\vec{k}_i, \omega_i) \cos(\vec{k}_i \cdot \vec{r} - \omega_i t) \end{aligned}$$

or

$$\begin{aligned}\vec{P}_{ind}(\vec{r}, t, \vec{Q}) = & \frac{1}{2} \left(\frac{\partial \chi}{\partial \vec{Q}} \right)_0 \vec{Q}(\vec{q}, \omega_0) \vec{E}_i(\vec{k}_i, \omega_i) \\ & \times \left\{ \cos \left[\left(\vec{k}_i + \vec{q} \right) \cdot \vec{r} - (\omega_i + \omega_0) t \right] \right. \\ & \left. + \cos \left[\left(\vec{k}_i - \vec{q} \right) \cdot \vec{r} - (\omega_i - \omega_0) t \right] \right\}\end{aligned}\quad (2.6)$$

Two different sinusoidal waves compose the induced polarization, one with wavevector $\vec{k}_S = (\vec{k}_i - \vec{q})$ and frequency $\omega_S = (\omega_i - \omega_0)$ which is the Stokes-shifted wave and the other with wavevector $\vec{k}_{AS} = (\vec{k}_i + \vec{q})$ and frequency $\omega_{AS} = (\omega_i + \omega_0)$ which is the anti-Stokes-shifted wave.

2.2.2 Quantum Theory

Quantum mechanics can, of course, be used to explain the Raman effect more completely. In the initial state $|i\rangle$ (before scattering occurs) there are $N_i(\omega_i)$ and $N_i(\omega_s)$ photons at the frequencies ω_i and ω_s , respectively. There are also $N_i(q)$ phonons present in the semiconductor while the electrons are all in their ground states. After a Stokes Raman scattering event, the system will be in the final state $|f\rangle$, with all the electrons remaining in the ground state and $N_f(\omega_i) = N_i(\omega_i) - 1$ incident photons, $N_f(\omega_s) = N_i(\omega_s) + 1$ scattered photons, $N_f(q) = N_i(q) + 1$ phonons. After an anti-Stokes scattering event, the final state $|f\rangle$ still has all the electrons in the ground state, and $N_f(\omega_i) = N_i(\omega_i) - 1$ incident photons, $N_f(\omega_s) = N_i(\omega_s) + 1$ scattered photons, but $N_f(q) = N_i(q) - 1$ phonons.

At first sight it seems that this scattering process does not involve electrons and therefore it can be described by an interaction Hamiltonian involving photons and phonons only. However, the strength of this interaction is very weak unless the photons and phonons have comparable frequency. Although such direct inelastic scattering of photons by phonons has been proposed theoretically [120], it has not been identified experimentally. Actually the electrons can couple to pho-

tons via the electron-radiation interaction Hamiltonian $\mathcal{H}_{\text{e-R}}$, and are involved in the scattering process as follows: *Step 1.* The incident photon excites the semiconductor into an intermediate state $|a\rangle$ by creating an electron-hole pair (or exciton). *Step 2.* This electron-hole pair is scattered into another state $|b\rangle$ by emitting a phonon via the electron-phonon interaction Hamiltonian $\mathcal{H}_{\text{e-ion}}$. *Step 3.* The electron-hole pair in $|b\rangle$ recombines radiatively with emission of the scattered photon.

In this way electrons mediate the Raman scattering of phonons although they remain unchanged after the process. One can draw a Feynman diagram involving the interactions between electrons, photons, and phonons during a Raman scattering event. Figure 2.2 shows all six Feynman diagrams representing possible

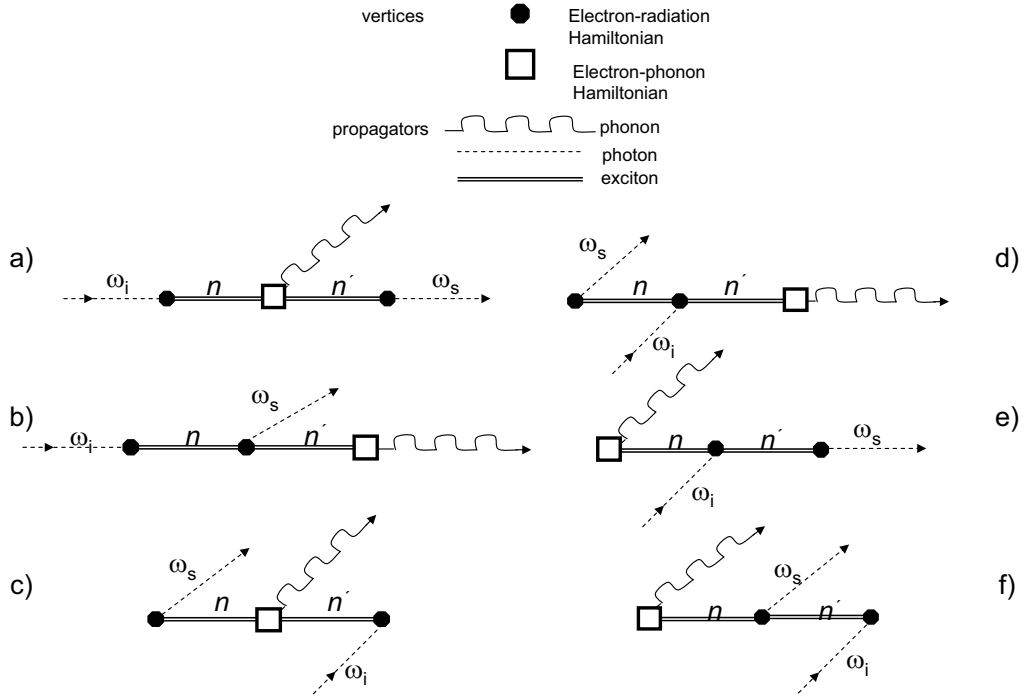


Figure 2.2: Feynman diagrams for the six scattering processes that contribute to Stokes Raman scattering. Graphs are duplicated from reference [118].

scattering processes. In each diagram lines lead from excitations (propagators)

into interactions (vertices). Arrows represent propagators, indicating creation (an arrow pointing away from a vertex) or annihilation (an arrow pointing towards a vertex) in an interaction. Any process can be derived from any other by permutating the time order of the vertices, therefore discussion of one diagram can be applied to another easily. Taking the process described in part (a) of the figure as an example, since each vertex in the Feynman diagram represents an interaction, the probability of the interaction can be derived from the Fermi Golden rule and will have the general form:

$$P \propto \left| \sum_n \frac{\langle n | \mathcal{H} | i \rangle}{[\hbar\omega_i - (E_n - E_i)]} \right|^2 \quad (2.7)$$

where $|i\rangle$ is the initial state with energy E_i , $|n\rangle$ is an intermediate electronic state with energy E_n , and \mathcal{H} is the Hamiltonian describing a particular interaction between states $|i\rangle$ and $|n\rangle$. By stepping through the interactions in figure 2.2 (a), one can write down the probabilities for successive vertices. Multiplying the probabilities for three processes in figure 2.2 (a) together yields the probability for the transition from initial state $|i\rangle$ to final state $|f\rangle$:

$$P = \left(\frac{2\pi}{\hbar} \right) \left| \sum_{n,n'} \frac{\langle f | \mathcal{H}_{\text{e-R}}(\omega_s) | n' \rangle \langle n' | \mathcal{H}_{\text{e-ion}}(\omega_o) | n \rangle \langle n | \mathcal{H}_{\text{e-R}}(\omega_i) | i \rangle}{\Delta E_1 \Delta E_2 \Delta E_3} \right|^2 \quad (2.8)$$

$$\Delta E_1 = [\hbar\omega_i - (E_n - E_i)] \quad (2.9)$$

$$\Delta E_2 = [\hbar\omega_i - (E_n - E_i) - \hbar\omega_o - (E_{n'} - E_n)] \quad (2.10)$$

$$\Delta E_3 = [\hbar\omega_i - (E_n - E_i) - \hbar\omega_o - (E_{n'} - E_n) - \hbar\omega_s - (E_f - E_{n'})] \quad (2.11)$$

where $\mathcal{H}_{\text{e-R}}$ is the Hamiltonian for the electron-radiation interaction between the incident or scattered photon and the electrons of the system. $\mathcal{H}_{\text{e-ion}}$ is the electron-phonon interaction Hamiltonian which describes how an electron-hole pair is scattered when emitting a phonon. $|i\rangle$, $|n\rangle$, $|n'\rangle$, and $|f\rangle$ are the initial, possible intermediate and final states of the system. $\hbar\omega_i$ and $\hbar\omega_s$ are the energies

of the incident and scattered photons respectively while $\hbar\omega_o$ is the energy of the phonon.

Equation (2.8) can be simplified slightly. First, equation (2.10) can be written as $\Delta E_2 = [\hbar\omega_i - \hbar\omega_o - (E_{n'} - E_i)]$, while equation (2.11) becomes $\Delta E_3 = [\hbar\omega_i - \hbar\omega_o - \hbar\omega_s - (E_i - E_f)]$. As previously mentioned Raman scattering does not change the final state of the electrons of a system, so $E_i = E_f$ and equation (2.11) further simplifies to $\Delta E_3 = [\hbar\omega_i - \hbar\omega_o - \hbar\omega_s]$. This will vanish if energy is conserved in the scattering process, so one can replace this denominator factor with the delta function $\delta(\hbar\omega_i - \hbar\omega_o - \hbar\omega_s)$. This delta function further simplifies equation (2.10) since $\hbar\omega_i - \hbar\omega_o = \hbar\omega_s$, so $\Delta E_2 = \hbar\omega_s - (E_{n'} - E_i)$. Substituting these simplifications into equation (2.8) yields the final scattering probability for one possible Raman process:

$$P = \left(\frac{2\pi}{\hbar}\right) \left| \sum_{n,n'} \frac{\langle i | \mathcal{H}_{e-R}(\omega_s) | n' \rangle \langle n' | \mathcal{H}_{e-ion}(\omega_o) | n \rangle \langle n | \mathcal{H}_{e-R}(\omega_i) | i \rangle}{[\hbar\omega_i - (E_n - E_i)] [\hbar\omega_s - (E_{n'} - E_i)]} \right|^2 \times \delta(\hbar\omega_i - \hbar\omega_o - \hbar\omega_s) \quad (2.12)$$

The other five possible processes (as indicated in figure 2.2) can be studied by repeating this procedure. Summing up all the results yields the total probability for Stokes Raman scattering.

2.2.3 Temperature Effects

Macroscopically, temperature will affect a crystal in two distinct manners, typically referred to as explicit and implicit temperature effects. How each of these effects changes the vibrational frequency of a Raman mode can be described as:

$$\left(\frac{\partial\nu}{\partial T}\right)_P = \left(\frac{\partial\nu}{\partial T}\right)_T - \left(\frac{\alpha}{\beta}\right) \left(\frac{\partial\nu}{\partial P}\right)_T \quad (2.13)$$

where

$$\alpha = \left(\frac{1}{V} \right) \left(\frac{\partial V}{\partial T} \right)_P$$

is the thermal expansivity of the material and

$$\beta = \left(\frac{1}{V} \right) \left(\frac{\partial V}{\partial P} \right)_T$$

is the compressibility of the material.

The phonon occupation number is used to measure the probability that a phonon state with energy $\hbar\nu$ is excited at a temperature T , and the first term in equation (2.13) is the explicit temperature effect related to changes in the phonon occupation number that occur with changes in temperature. The second term is the implicit temperature effect that quantifies the change in vibrational frequency due to thermal expansion and contraction of the crystal lattice.

From the quantum point of view, the temperature dependence of the phonon frequencies and linewidths can also be further explained by invoking the anharmonic interaction model. This was a popular research topic in the 1960–1980s, and several theoretical models for anharmonic decay of optical phonons have been developed, e.g., Cowley’s model [121, 122] and Klemens’ model [123], both of which were improved and used later to investigate the Raman effects in particular materials, such as Si, Ge, and α -Sn [124, 125]. Klemens used a simplified physical model to estimate the interaction strength of the optical mode with other lattice modes, while Cowley elaborated the interactions and summed them numerically.

Both Cowley’s and Klemens’ works were based on the anharmonic contribution to the Hamiltonian,

$$\begin{aligned}
\mathcal{H}_A = & \sum_{\vec{q}_1, \vec{q}_2, \vec{q}_3} \sum_{j_1, j_2, j_3} V \begin{pmatrix} \vec{q}_1 & \vec{q}_2 & \vec{q}_3 \\ j_1 & j_2 & j_3 \end{pmatrix} A(\vec{q}_1, j_1) A(\vec{q}_2, j_2) A(\vec{q}_3, j_3) \\
& + \sum_{\vec{q}_1, \vec{q}_2, \vec{q}_3, \vec{q}_4} \sum_{j_1, j_2, j_3, j_4} V \begin{pmatrix} \vec{q}_1 & \vec{q}_2 & \vec{q}_3 & \vec{q}_4 \\ j_1 & j_2 & j_3 & j_4 \end{pmatrix} \\
& \quad \times A(\vec{q}_1, j_1) A(\vec{q}_2, j_2) A(\vec{q}_3, j_3) A(\vec{q}_4, j_4) \\
& + \dots
\end{aligned} \tag{2.14}$$

where \vec{q} is the wave vector and j is the lattice index, and

$$A(\vec{q}, j) = a_{-\vec{q}, j}^\dagger + a_{\vec{q}, j}$$

the a 's being the usual phonon creation and annihilation operators. The effect of these anharmonic interactions on the Raman-allowed optical mode is to change its harmonic frequency $\omega(\vec{0}, j)$ to a damped frequency $\omega(\vec{0}, j; \Omega)$ given by

$$\omega^2(\vec{0}, j; \Omega) = \omega^2(\vec{0}, j) + 2\omega(\vec{0}, j)[\Delta(\vec{0}, j; \Omega) + i\Gamma(\vec{0}, j; \Omega)] \tag{2.15}$$

The real and imaginary parts of materials' self-energy, $\Delta(\vec{0}, j; \Omega)$ and $\Gamma(\vec{0}, j; \Omega)$ are usually much smaller than $\omega(\vec{0}, j)$ and equation (2.15) can be rewritten as

$$\omega(\vec{0}, j; \Omega) = \omega(\vec{0}, j) + \Delta(\vec{0}, j; \Omega) + i\Gamma(\vec{0}, j; \Omega) \tag{2.16}$$

Thus the line shape of the Stokes Raman peak becomes

$$I_s(\vec{0}, j; \Omega) \propto \frac{\Gamma(\vec{0}, j; \Omega)}{[\omega(\vec{0}, j) + \Delta(\vec{0}, j; \Omega) - \Omega]^2 + \Gamma^2(\vec{0}, j; \Omega)} [n(\Omega) + 1] \tag{2.17}$$

with the thermal occupation number

$$n(\Omega) = \frac{1}{\exp(\hbar\Omega/kT) - 1} \quad (2.18)$$

The function $\Delta(\vec{0}, j; \Omega)$ gives the shift of the peak position. The three lowest-order contributions to the expansion of the self-energy yield

$$\begin{aligned} \Delta(\vec{0}, j; \Omega) = & \Delta^{(0)} + \frac{12}{\hbar} \sum_{\vec{q}, j'} V \begin{pmatrix} \vec{0} & \vec{0} & q & -q \\ j & j & j' & j' \end{pmatrix} [2n(\vec{q}, j') + 1] \\ & - \frac{18\pi}{\hbar^2} \sum_{\vec{q}, j_1, j_2} \left| V \begin{pmatrix} \vec{0} & \vec{q} & -\vec{q} \\ j & j_1 & j_2 \end{pmatrix} \right|^2 [n(\vec{q}, j_1) + n(-\vec{q}, j_2) + 1] \\ & \times \left[\frac{1}{\omega(\vec{q}, j_1) + \omega(\vec{q}, j_2) - \Omega} \right]_P \end{aligned} \quad (2.19)$$

with $n(\vec{q}, j) = n(\omega(\vec{q}, j))$ given in equation (2.18). The first term in equation (2.19) is the thermal-expansion contribution to the line shift. It may be written as

$$\Delta^{(0)} = \omega(\vec{0}, j) \exp \left[-3\gamma(\vec{0}, j) \int_0^T \alpha(T') dT' \right] \quad (2.20)$$

where $\alpha(T)$ is the coefficient of linear thermal expansion mentioned above and $\gamma(\vec{0}, j)$ is the Grüneisen parameter for the optical Raman mode.

The broadening of the Raman line is given by

$$\begin{aligned} \Gamma(\vec{0}, j; \Omega) = & \frac{18\pi}{\hbar^2} \sum_{\vec{q}, j_1, j_2} \left| V \begin{pmatrix} \vec{0} & \vec{q} & -\vec{q} \\ j & j_1 & j_2 \end{pmatrix} \right|^2 [n(\vec{q}, j_1) + n(-\vec{q}, j_2) + 1] \\ & \times \delta(\omega(\vec{q}, j_1) + \omega(-\vec{q}, j_2) - \Omega) \end{aligned} \quad (2.21)$$

The physical meaning of equation (2.21) is transparent: Owing to the anharmonic interactions the optical Raman phonon decays in a combination of two phonons

$\omega(\vec{q}, j_1)$ and $\omega(-\vec{q}, j_2)$ satisfying $\omega(\vec{q}, j_1) + \omega(-\vec{q}, j_2) = \Omega$. The matrix elements which determine the width $\Gamma(\Omega)$ are given by

$$\begin{aligned}
V \begin{pmatrix} \vec{0} & \vec{q} & -\vec{q} \\ j & j_1 & j_2 \end{pmatrix} &= \frac{1}{6} \left[\frac{\hbar^3}{8NM^3\omega_0\omega(q, j_1)\omega(-q, j_2)} \right]^{1/2} \\
&\times \sum_{l', l''} \sum_{k, k', k''} \sum_{\alpha, \beta, \gamma} \phi_{\alpha\beta\gamma} \begin{pmatrix} 0 & l' & l'' \\ k & k' & k'' \end{pmatrix} \\
&\times e_\alpha \left(k \middle| \vec{0}, j \right) e_\beta \left(k' \middle| \vec{q}, j_1 \right) e_\gamma \left(k'' \middle| -\vec{q}, j_2 \right) e^{i\vec{q}[\vec{R}(l') - \vec{R}(l'')]}
\end{aligned} \tag{2.22}$$

where

$$\phi_{\alpha\beta\gamma} \begin{pmatrix} 0 & l' & l'' \\ k & k' & k'' \end{pmatrix}$$

is the third derivative of the interatomic potential with respect to displacements along directions of the Cartesian coordinates α , β , and γ of the atoms

$$\begin{pmatrix} 0 \\ k \end{pmatrix}, \begin{pmatrix} l' \\ k' \end{pmatrix}, \begin{pmatrix} l'' \\ k'' \end{pmatrix}$$

respectively. The index l labels the primitive cells and k labels the position of the two atoms within the primitive cell. The vectors $\vec{e}(k|\vec{q}, j)$ are the eigenvectors of the harmonic problem. M is the atomic mass and N the number of cells in the crystal.

Here we follow Klemens' method to evaluate equation (2.21). Klemens assumes that the optical Raman phonon decays into two acoustical phonons of opposite \vec{q} belonging to the same branch. This means $j_1 = j_2$ in equation (2.21) which leads to $\omega(\vec{q}, j_1) = \omega(-\vec{q}, j_2)$. Therefore one obtains the Raman line shape broadening in the form

$$\Gamma(\omega_0, T) = \Gamma(\omega_0, 0) [1 + 2n(\omega_0/2)] \quad (2.23)$$

The constant $\Gamma(\omega_0, 0)$, which is the Raman line width at zero temperature, can be determined by making further approximations to compute the matrix elements and the density of states. However, Klemens' model yields much smaller Raman line widths than the experimental data in several typical materials such as diamond, Si, Ge, and α -Sn. On the other hand, more accurate $\Gamma(\omega_0)$ values for diamond have been achieved by Cowley's calculations, in which he solved the harmonic problem with a shell model and assumed the anharmonic contribution to be an axially symmetric force between nearest neighbors. The calculated Γ 's for Si and Ge in this method are larger than the experimental results by a factor of ~ 10 , and this discrepancy arises mainly from the poor description of the phonon dispersion curves by the shell model.

As indicated by equations (2.19) and (2.23), increasing the temperature of a material will increase the thermal occupation number $n(\Omega)$, causing Raman lines both to broaden and to shift to lower frequency. Furthermore this broadening and shifting change with temperature should be gentle and smooth (no abrupt change), as shown in figure 2.3 which are the frequency and FWHM evolutions with temperature in several typical materials (Si, Ge, α -Sn). In addition, as the temperature goes up the lengths of the weak intermolecular van der Waals force bonds change more than those of the intramolecular covalent bonds during thermal expansion, therefore intermolecular modes will undergo more change than will intramolecular modes with temperature.

2.3 Experimental Setup

In my experiments, I recorded the Raman spectra using a Dilor XY triple spectrometer in a backscattering configuration in which the scattered light was

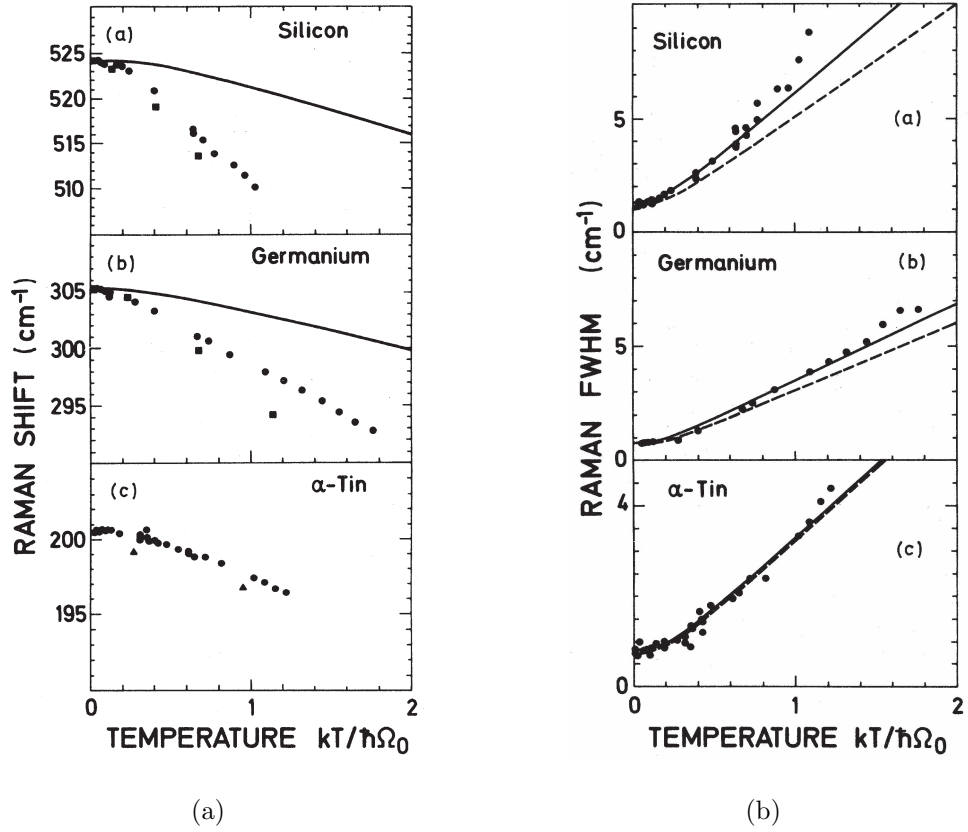


Figure 2.3: (a) Sample Raman frequency shift as a function of the normalized temperature $kT/\hbar\Omega_0$ in Si, Ge and α -Sn. Solid lines in the graphs for Si and Ge are the thermal-expansion contribution to the line shift. Squares represent Cowley's calculation plus the effect of thermal expansion; (b) Sample Raman line widths as a function of the normalized temperature. Dotted line is the prediction of Klemens' model. Ω_0 is the Raman frequency for $T \rightarrow 0$. Graphs are duplicated from reference [125].

collected using a charge-coupled device (CCD) cooled with liquid nitrogen. The resolution of the spectrometer is 1 cm^{-1} . The schematic for the system that I used to collect the signals is shown in figure 2.4.

I selected large sample pieces from the same crystal growth run for each kind of material, but used different crystals for different experiments. I collected data for each sample over the spectral range of approximately 25 cm^{-1} to 1600 cm^{-1} , to include both inter- and intramolecular vibrations. However, I found that the intermolecular vibrations were of more interest since they were more sensitive to

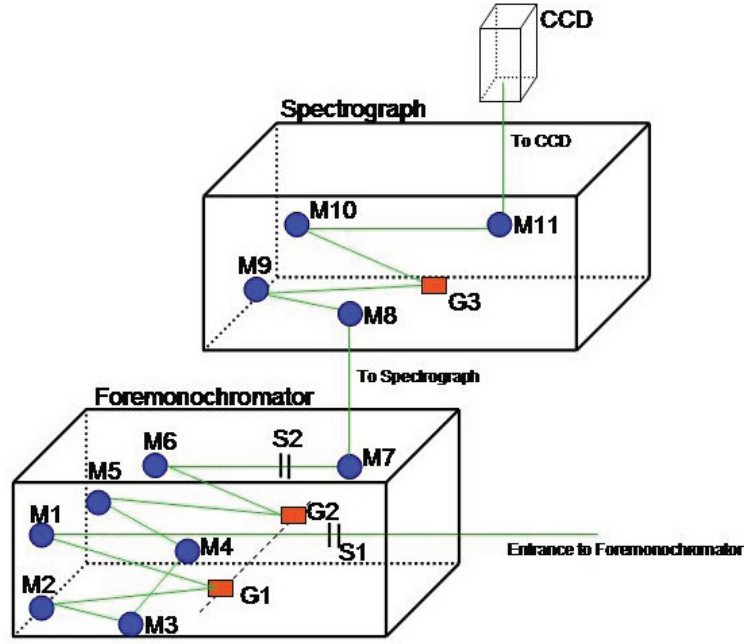


Figure 2.4: Raman Spectrometer Schematic. M1–M11 are mirrors, G1–G3 are gratings and S1–S2 are slits in the system.

changes in external conditions such as temperature.

In the room-temperature experiments, I put the samples on a glass slide under the microscope, with their *bc*-planes perpendicular to the incident laser beam (micro-Raman setup). The diphenylanthracene samples are needle-like with the *a*-axis coinciding with the axis of the needle, so the incident beam was perpendicular to the *a*-axis but the orientation of the crystals was not otherwise controlled. The incident laser was focused on the sample surface.

In temperature-dependent experiments, the samples, as well as the cryogenic chamber in which they were sealed, were placed in the laser path outside the spectrograph (macro-Raman setup), such that the scattered signals could go back in opposite direction and be collected by spectrometer. I placed the factory-made camera lens with focal length $f = 5$ cm right at the macro-Raman exit, as well as two extra lenses with $f = 5$ cm and 10 cm in front of the samples to help the laser alignment. I configured the optical lens system such that laser was focused on the samples ~ 30 cm away from the macro-Raman exit, and the scattered light

was directed perpendicular to slit 1 in figure 2.4 to maximize the light collection.

To load the samples in low-temperature experiments, I utilized a specially-designed square-shaped holder which was approximately 1.3×1.5 cm in dimension and coated with gold to assure high thermal conductivity. In the center of the holder there was a circular hole whose diameter was approximately 1.0 cm. I mounted the samples using a small amount of vacuum grease at the edge of the hole, again with their *bc*-planes perpendicular to the incident laser beam. In this way I could make sure the incident laser would hit the crystals themselves without interference from the grease or substrates.

I attached the holder together with all the samples on it to the lower end of the cryostat's cold finger, filling the space between with pure indium. A wire heater on the cold finger allowed me to change the temperature. A platinum resistance thermometer (PRT) on the cold finger, which responded to the temperature change by varying its electric resistance, was in intimate contact with the sample holder at the left-upper corner. I covered the cold finger with a thermo-shield, and sealed the cryogenic chamber. I pumped the chamber down to approximately 10^{-6} Torr with a diffusion pump vacuum system, and was then able to cool the crystals to as low as 30 K with an Air Products closed-cycle He refrigerator.

I used a LakeShore temperature controller DRC-82C to control the temperature of the crystals. By adjusting the voltage and gain applied to the heater, it is possible to increase or decrease its power output, and eventually change the temperature in the chamber. The approximate maximum power and resistance of the heater is 25 W and 25Ω , therefore I was very careful to hold the voltage not to exceed 25 V. Once the temperature approached the desired value, I turned down the voltage gain slowly until heating and cooling reached an approximate equilibrium. In all measurements the temperatures were fine-tuned to fluctuate within a ± 2 K range.

Rubrene is known to highly favor creating a peroxide layer in the presence of light and oxygen [126,127], as mentioned above. I made no attempts to keep the

crystals dry or in the dark, thus the collected data may have included spectra from both the underlying bulk rubrene crystal and the surface peroxide layer.

I used a tunable wavelength laser system to excite the crystals. For those with band gaps larger than photon energy (2.4 eV) of the argon green line, such as anthracene, tetracene, pentacene, and diphenylanthracene, I used a Spectra-Physics 2017 Ar⁺ laser which generates a green laser line of 514.5 nm wavelength; while for rubrene, I used the Ar⁺ laser to pump a Spectra-Physics 375B dye laser with Kiton Red dye, which yielded an output energy in a continuously tunable range from 608 to 711 nm (2.04–1.74 eV). I chose to use a single excitation wavelength of 650.45 nm (1.906 eV) in the experiments to minimize the photoluminescence from the sample.

The integration time for each scan depended on the laser intensity in use, but I chose it to maximize the signal-to-noise ratio while protecting the CCD from saturation from the background luminescence. I also collected the data with the incident laser reflected only by a white board (“flat” condition) and with no incident or environment light at all (“dark” condition), and then used the method

$$data_{calibrated} = \frac{data_{measured} - data_{dark}}{data_{flat} - data_{dark}}$$

to deconvolve the samples’ spectra from equipment effects such as the non-linear response of the CCD. This way the backgrounds were subtracted, and all peaks were fitted using Lorentzian lineshapes with a least-squares algorithm in the Origin Pro software.

2.4 Calculations Based on Density Functional Theory

Density functional theory (DFT) is a quantum-mechanical approach used in physics and chemistry to investigate the electronic structure (principally the ground state) of many-body systems, such as atoms and molecules. In this theory the most important physical parameter is the spatially-dependent electron density; other properties of a many-electron system can be determined by using functionals, i.e., functions of the electron density function. To calculate the electronic structures, one can begin with the Schrödinger equation:

$$\mathcal{H}\Psi = E\Psi \quad (2.24)$$

where E is the electronic energy, $\Psi = \Psi(\vec{r}_1, \vec{r}_2, \dots, \vec{r}_n)$ is the wave function, and \mathcal{H} is the Hamiltonian operator,

$$\mathcal{H} = \hat{T} + \hat{V}_{ne} + \hat{V}_{ee} \quad (2.25)$$

where

$$\hat{T} = \sum_{i=1}^N \left(-\frac{\hbar^2}{2m} \nabla_i^2 \right)$$

is the kinetic energy operator (N being the number of electrons),

$$\hat{V}_{ne} = \sum_{i=1}^N V(\vec{r}_i)$$

is the electron-nucleus attraction energy operator, and

$$\hat{V}_{ee} = \sum_{i<j}^N U(\vec{r}_i, \vec{r}_j)$$

is the electron-electron repulsion energy operator. Therefore the Schrödinger equation becomes

$$\left[\sum_{i=1}^N \left(-\frac{\hbar^2}{2m} \nabla_i^2 \right) + \sum_{i=1}^N V(\vec{r}_i) + \sum_{i<j}^N U(\vec{r}_i, \vec{r}_j) \right] \Psi = E\Psi \quad (2.26)$$

On the other hand the electron density $n(\vec{r})$ is related to a normalized Ψ by

$$n(\vec{r}) = N \int d^3r_2 \int d^3r_3 \cdots \int d^3r_N \Psi^*(\vec{r}, \vec{r}_2, \cdots, \vec{r}_n) \Psi(\vec{r}, \vec{r}_2, \cdots, \vec{r}_n) \quad (2.27)$$

It has been shown that this relation can be reversed, i.e., for a given ground-state density $n_0(\vec{r})$ it is possible to calculate the corresponding ground-state wavefunction $\Psi_0(\vec{r}_1, \vec{r}_2, \cdots, \vec{r}_n)$ [128]. In other words, Ψ_0 is a unique functional of n_0 ,

$$\Psi_0 = \Psi(n_0)$$

so that the ground-state expectation value of an observable \mathcal{O} is a functional of n_0

$$O(n_0) = \langle \Psi(n_0) | \mathcal{O} | \Psi(n_0) \rangle$$

and of course the ground state energy of a molecular system is also a functional of n_0

$$\begin{aligned} E_0 &= E(n_0) \\ &= \left\langle \Psi(n_0) \left| \hat{T} + \hat{V}_{ne} + \hat{V}_{ee} \right| \Psi(n_0) \right\rangle \\ &= \left\langle \Psi(n_0) \left| \hat{T} \right| \Psi(n_0) \right\rangle + \left\langle \Psi(n_0) \left| \hat{V}_{ne} \right| \Psi(n_0) \right\rangle + \left\langle \Psi(n_0) \left| \hat{V}_{ee} \right| \Psi(n_0) \right\rangle \quad (2.28) \end{aligned}$$

Assuming that the nuclei of the molecules or clusters are fixed (the Born-Oppenheimer approximation), we call \hat{T} and \hat{V}_{ne} universal operators as they are the same for any system, while \hat{V}_{ee} is system-dependent, thus called non-universal. More generally, the contribution of $\langle \Psi | \hat{V}_{ee} | \Psi \rangle$ can be written as

$$V_{ee}(n) = \int \hat{V}_{ee}(\vec{r}) n(\vec{r}) d^3r$$

One can therefore write down the total energy of a system

$$E(n) = T(n) + V_{ne}(n) + \int \hat{V}_{ee}(\vec{r}) n(\vec{r}) d^3r \quad (2.29)$$

It is apparent that it is a function of electron density n , and can be minimized with respect to n . A successful minimization of the energy functional will yield the ground-state density n_0 and thus all other ground-state observables.

In my research, I performed the DFT calculation with the B3LYP method and the 6-311G(d) basis set, in GAUSSIAN 03 software on an SGI Origin 3800 with 64 CPUs and 128 GB memory running the IRIX 6.5 operating system. Starting from the experimental X-ray structures, I was able to calculate the vibrational modes of a isolated molecule and the minimum energies of pairs of molecules with different point groups. For those materials for which we lacked the X-ray data, I performed the computations with the “ideal symmetry” structures.

Chapter 3

Molecular Vibration in Oligoacenes and Oligoacene Derivatives

I compare the Raman spectra of three oligoacene single crystals (anthracene, tetracene and pentacene) and one oligoacene derivative single crystal (diphenyl anthracene) with the calculated spectra of the respective isolated molecules. The Raman measurements I present here are of the bulk properties of the material and confirm that the vapor growth process yields very pure, unstrained crystals. They indicate that oligoacenes have strong intermolecular coupling and show observable modes in the low-frequency wavenumber range, the strengths of which decrease as the fused benzene rings stack. On the other hand diphenylanthracene (DPA) shows relatively weak intermolecular vibrational modes, as well as some intramolecular ones in the low-frequency range, because the side phenyl groups in the DPA molecules prevent close packing with the neighboring molecules.

3.1 The Crystals

Anthracene, tetracene and pentacene are relatively small aromatic hydrocarbons consisting of 3, 4, and 5 fused benzene rings respectively, as shown in figure 1.1. Diphenylanthracene (DPA) is a derivative of anthracene (as its name suggests), with two side phenyl groups linked to the central benzene ring, one on each side, and its structure is shown in figure 1.2. Christian Kloc grew the single crystals of these materials when he was at Lucent Technologies, by horizontal physical vapor transport in a flow of argon gas starting with commercially available powders, and the method is described in reference [111]. He also combined some previously-sublimed crystals and performed vacuum-sealed ampoule growth to get thick bulk crystallites more suitable for the measurements presented here.

All the three oligoacene materials, i.e., anthracene, tetracene, and pentacene, crystallize in a triclinic structure and have C_i point group symmetry with two molecules in the unit cell. The lattice constants for the triclinic unit cells are: $|\vec{a}| = 8.56 \text{ \AA}$, $|\vec{b}| = 6.04 \text{ \AA}$, and $|\vec{c}| = 11.16 \text{ \AA}$ for anthracene [129]; $|\vec{a}| = 7.98 \text{ \AA}$, $|\vec{b}| = 6.14 \text{ \AA}$, and $|\vec{c}| = 13.57 \text{ \AA}$ for tetracene [62]; and $|\vec{a}| = 7.93 \text{ \AA}$, $|\vec{b}| = 6.14 \text{ \AA}$, and $|\vec{c}| = 16.03 \text{ \AA}$ for pentacene [62]. DPA crystallizes in a monoclinic structure and has C_2/c point group symmetry with four molecules in the unit cell. The lattice constants for the monoclinic unit cell are: $|\vec{a}| = 10.7 \text{ \AA}$, $|\vec{b}| = 13.6 \text{ \AA}$, and $|\vec{c}| = 12.3 \text{ \AA}$ [130].

Figure 3.1 illustrates the structure of the anthracene molecule with some carbon atoms labeled. I also perform an optimization calculation using the method described in section 2.4, and compare the results with the experimental geometrical structure in table 3.1. My colleague and my collaborator, Drs. Weinberg-Wolf and Liu, have performed the calculations for tetracene, and their results are duplicated in table 3.2. The comparisons of the experimental and theoretical geometrical structures of the pentacene and DPA molecules are also listed in tables 3.3 and 3.4. As can be seen from tables 3.1–3.4, my optimization calcula-

tions simulate the molecular structures of different kinds of materials very well, therefore the results are reliable and can be used as a starting point for further Raman spectra simulation.

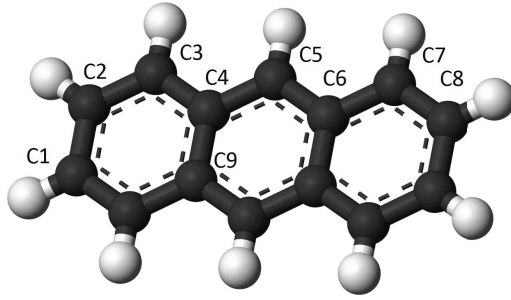


Figure 3.1: Anthracene ($C_{14}H_{10}$) Molecule. The labels on the carbon atoms refer to table 3.1.

Table 3.1: Comparison of experimental and theoretical geometrical structures of the anthracene molecule. Refer to the atomic labeling scheme in figure 3.1.

	Experiment*	Theory
Distances		
C1-C2	1.390 Å	1.401 Å
C2-C3	1.361 Å	1.382 Å
C3-C4	1.426 Å	1.415 Å
C4-C5	1.387 Å	1.391 Å
C5-C6	1.395 Å	1.408 Å
C6-C7	1.412 Å	1.396 Å
C7-C8	1.366 Å	1.387 Å
C4-C9	1.440 Å	1.401 Å

* See reference [129]

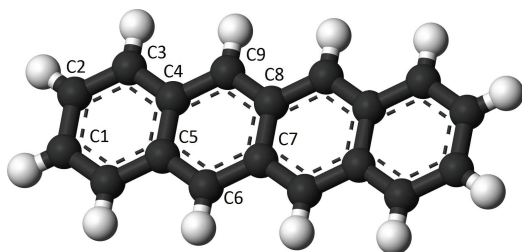


Figure 3.2: Tetracene ($C_{18}H_{12}$) Molecule. The labels on the carbon atoms refer to table 3.2.

Table 3.2: Comparison of experimental and theoretical geometrical structures of the tetracene molecule. Refer to the atomic labeling scheme in figure 3.2.

	Experiment*	Theory
Distances		
C1-C2	1.431 Å	1.420 Å
C2-C3	1.367 Å	1.365 Å
C3-C4	1.434 Å	1.427 Å
C4-C5	1.452 Å	1.452 Å
C7-C8	1.452 Å	1.455 Å
C8-C9	1.410 Å	1.395 Å
C4-C9	1.393 Å	1.391 Å

* See reference [131]

Table 3.3: Comparison of experimental and theoretical geometrical structures of the pentacene molecule. Refer to the atomic labeling scheme in figure 3.3.

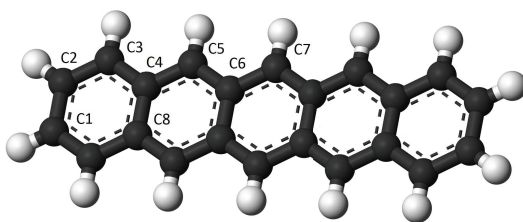


Figure 3.3: Pentacene ($C_{22}H_{14}$) Molecule. The labels on the carbon atoms refer to table 3.3.

	Experiment*	Theory
Distances		
C1-C2	1.43 Å	1.415 Å
C2-C3	1.38 Å	1.393 Å
C3-C4	1.43 Å	1.427 Å
C4-C5	1.40 Å	1.396 Å
C5-C6	1.42 Å	1.402 Å
C6-C7	1.41 Å	1.417 Å
C4-C8	1.46 Å	1.446 Å

* See reference [132]

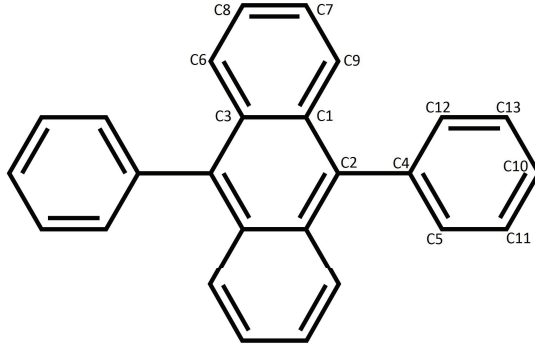


Figure 3.4: DPA ($C_{26}H_{18}$) Molecule. The labels on the carbon atoms refer to table 3.4.

Table 3.4: Comparison of experimental and theoretical geometrical structures of the DPA molecule. Refer to the atomic labeling scheme in figure 3.4.

	Experiment*	Theory
Distances		
C1-C2	1.36 Å	1.398 Å
C1-C3	1.50 Å	1.467 Å
C1-C9	1.42 Å	1.415 Å
C2-C4	1.56 Å	1.476 Å
C2-C3	1.39 Å	1.401 Å
C3-C6	1.41 Å	1.405 Å
C4-C5	1.35 Å	1.413 Å
C4-C12	1.34 Å	1.410 Å
C5-C11	1.43 Å	1.404 Å
C6-C8	1.33 Å	1.386 Å
C7-C8	1.48 Å	1.467 Å
C7-C9	1.30 Å	1.386 Å
C10-C11	1.33 Å	1.365 Å
C10-C13	1.44 Å	1.417 Å
C12-C13	1.39 Å	1.411 Å

* See reference [133]

3.2 Raman Spectra

I used multiple crystallites from the same growth batch at the same time for these room-temperature experiments, paying no deliberate attention to the orientation of the crystallites. Any polarization effects will therefore average over the entire group of crystals, which will affect the analysis of the data. I recorded spectra with the micro-Raman setup using a Dilor XY triple spectrometer in a backscattering configuration and a charge-coupled device (CCD) cooled with LN_2 . My spectral windows ranged from approximately 25 cm^{-1} to 1600 cm^{-1} with a resolution of 1 cm^{-1} , a range that should include both intermolecular and intramolecular vibrations. After subtracting the background, I fit all peaks using Lorentzian lineshapes with a least-squares algorithm. Studying multiple crystals also allowed me to investigate the consistency of crystals produced in a single growth run: I collected Raman spectra from several different platelet- and needle-like crystallites (as well as from multiple locations on some of the larger crystallites), and all of the spectra are substantially the same, other than small changes in the relative intensities of individual peaks. This is a strong indication that the crystal-growing process is creating very pure, unstrained crystals.

Figure 3.5 contains representative Raman spectra of anthracene, tetracene, pentacene, and DPA single crystals measured at room temperature. The spectrum of each material shows a few vibrational modes in the low-frequency range (below 200 cm^{-1}). One gains more information about the individual modes by comparing the spectra to calculations of the Raman modes of the isolated molecules. Such comparisons in the low-frequency range are of particular interest, because they distinguish the inter- and intramolecular vibrations easily.

The top line in figure 3.6 contains the comparison for anthracene single crystals. As can be seen, the four lowest-energy vibrations are not predicted by the calculation based on a single anthracene molecule. Actually the lowest intramolecular vibration predicted by the calculation is at $\sim 230\text{ cm}^{-1}$ with energy

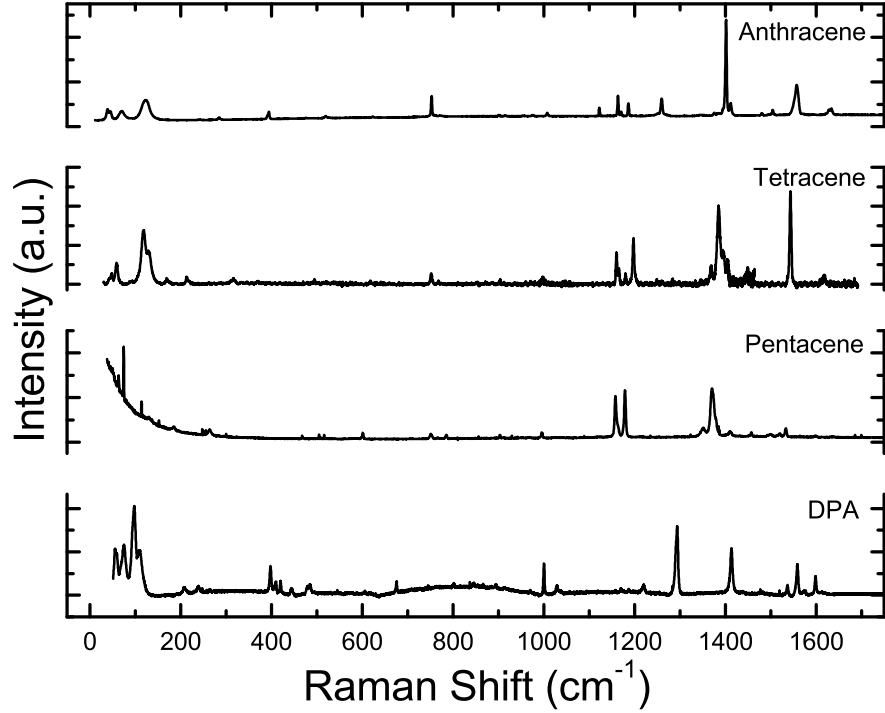


Figure 3.5: Representative room temperature (300 K) Raman spectrum of anthracene, tetracene, pentacene, and DPA single crystals, from top to bottom. Signals are collected with an excitation energy of 514.532 nm (2.4 eV).

28 meV, therefore energies smaller than that would only activate intermolecular vibrations. The calculation based on one tetracene molecule, as shown in the second line, has been analyzed before, and one can find a detailed comparison in reference [105]. In tetracene the lowest vibrational mode predicted by theory appears at $\sim 115 \text{ cm}^{-1}$ (14 meV), and intermolecular vibrations account for the two peaks below it. The third line is the comparison for pentacene single crystals. The calculation for pentacene predicts the lowest vibration at $\sim 100 \text{ cm}^{-1}$ (13 meV), and the two vibrations below 100 cm^{-1} probably come from intermolecular vibrations. Comparing anthracene, tetracene, and pentacene, one can see that the lowest energy for an intramolecular vibration decreases as the number of benzene rings in the backbone increases. The vibrational mode with smallest

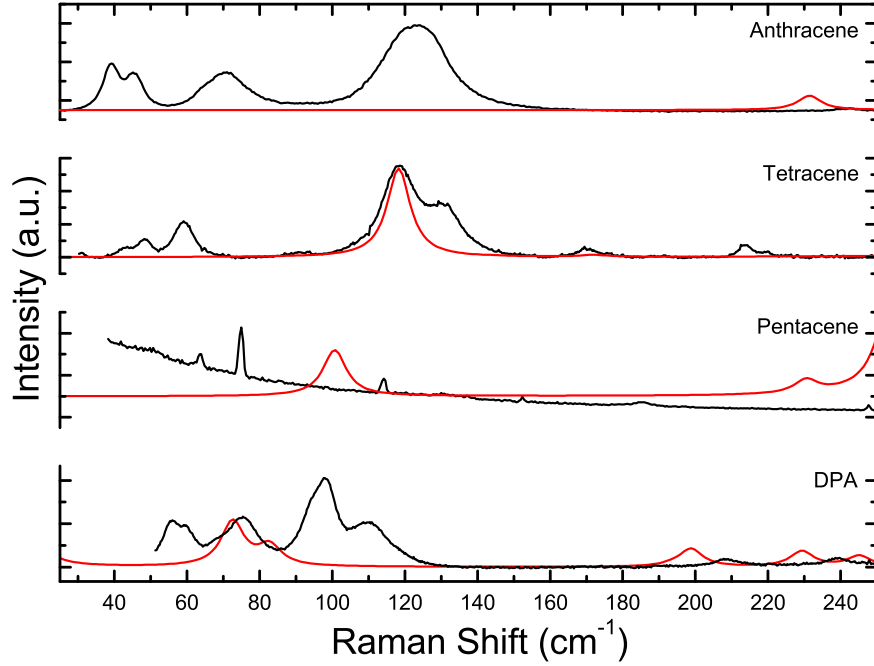


Figure 3.6: Room temperature low-energy experimental data and theoretical predictions for anthracene, tetracene, pentacene, and DPA single crystals, from top to bottom. Black line denotes experimental observation and red line denotes theoretical prediction.

energy in all three oligoacenes is the motion of benzene rings with two ends moving in the opposite directions perpendicular to the backbone plane, which looks like the propagation of a wave along the long axis direction of the molecule. The more benzene rings are fused, the more “flexible” this rings link is, and therefore needs smaller energy to activate the vibration.

As a contrast, the comparison between experimental data and theoretical predictions for DPA single crystals is illustrated in the bottom line. Two predicted peaks appear at $\sim 20 \text{ cm}^{-1}$ (2.5 meV, not shown in figure 3.6) and $\sim 75 \text{ cm}^{-1}$ (9 meV), both of which are related to the motion of side phenyl groups. Although the experimental spectrum below 30 cm^{-1} is overwhelmed by the laser tail, we can still come to the conclusion that some of the peaks in the low-frequency

range of DPA are predicted by the single-molecule calculation, however some aren't. The unit cell of DPA is almost four times as large as those of the three oligoacenes. While the DPA molecule itself is larger than the oligoacenes, it is mainly the differences in packing, and the fact that DPA has four molecules in the unit cell and the others only have two, that cause the change in the size of the unit cell. The phenyl groups on the DPA molecule prevent the close packing arrangement achieved by anthracene, tetracene, and pentacene in the solid state, and their motion is almost uncoupled from that of the backbone. For this reason, it is not surprising to find relatively weaker intermolecular interactions between DPA molecules, which probably come from the coupling of phenyl groups with the neighboring molecule.

3.3 Conclusion

I report room-temperature Raman spectra for three oligoacene materials, i.e., anthracene, tetracene, and pentacene, as well as an oligoacene derivative material, i.e., diphenylanthracene. There exist intermolecular interactions in oligoacenes, and the coupling strengths decrease as the molecules become larger. The molecule of DPA is larger than those of the oligoacenes, and the side phenyl groups prevent close packing, therefore intermolecular interactions are even weaker in DPA than they are in other molecular crystals. I compare the experimental Raman spectra with calculated results based on isolated molecules, and catalog those peaks below 200 cm^{-1} that are not predicted by the theory as intermolecular vibrations. The comparisons confirm that the DFT method that I use is a reliable one, which generates bond lengths close to experimental values in molecules.

Chapter 4

Molecular Vibration in Rubrene: Raman Study and A New Model

I perform temperature-dependent Raman measurements on single crystals of rubrene. The Raman spectra I present here are of the bulk properties of the material and confirm that the vapor growth process yields very pure, unstrained rubrene crystals. At temperatures below 80 K they display two weak intermolecular vibrations in the very low-frequency region (below 60 cm^{-1}), which red-shift rapidly with increasing temperature until they become undetectable (below 20 cm^{-1}). Other Raman peaks in the low-frequency region ($60\text{--}150\text{ cm}^{-1}$) undergo significant line width broadening over the temperature range from 30–300 K, especially between 150–200 K, indicating a shortening of the lifetime of the vibrational modes corresponding to these peaks. I propose a new model to ascribe this to breaking of the symmetry of the molecular motion, and performed DFT calculations to support this theory.

4.1 The Rubrene Crystal

Rubrene is a relatively small aromatic hydrocarbon consisting of a backbone of four fused benzene rings (tetracene) with four substituted phenyl groups (two

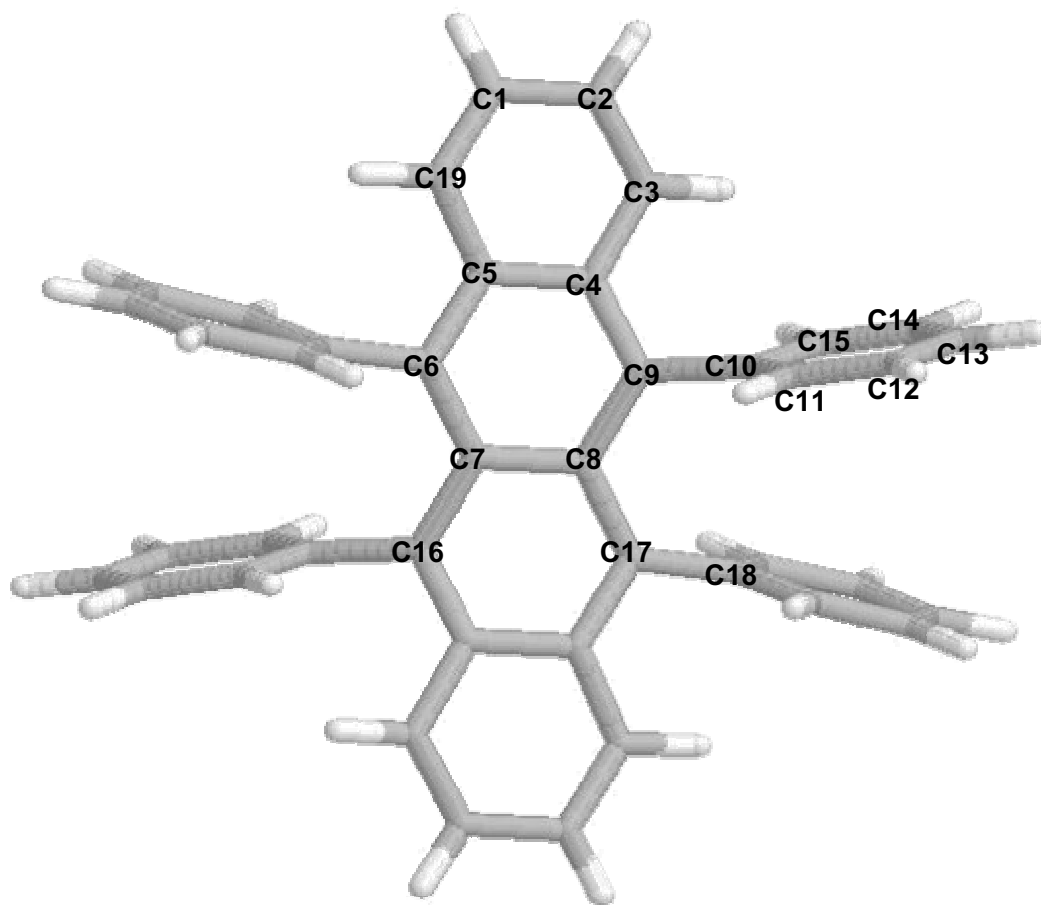


Figure 4.1: Rubrene ($C_{42}H_{28}$) molecule. The labels on the carbon atoms are in reference to table 4.1.

on each internal ring). Figure 4.1 illustrates the structure of rubrene molecule, and table 4.1 shows the comparison between experimental atom positions and those from calculation by the method described in section 2.4.

Dr. Christian Kloc grew the single crystals used in these measurements by horizontal physical vapor transport in a flow of argon gas starting with rubrene powder acquired from Aldrich. Other publications describe the details of this growth process [112]. To change the morphology of the growing crystals and to get thick bulk crystallites more suitable for this present study, some previously-sublimed rubrene crystals subsequently served as the starting point for a typical vacuum-sealed ampoule growth. The molecule crystallizes in an orthorhombic

Table 4.1: Comparison of experimental and theoretical geometrical structures of rubrene molecule. Refer to the atomic labeling scheme in figure 4.1.

	Experiment*	Theory
Distances		
C1-C2	1.442 Å	1.408 Å
C2-C3	1.366 Å	1.351 Å
C3-C4	1.439 Å	1.433 Å
C4-C5	1.466 Å	1.440 Å
C7-C8	1.474 Å	1.464 Å
C8-C9	1.431 Å	1.418 Å
C4-C9	1.409 Å	1.397 Å
C9-C10	1.503 Å	1.506 Å
C10-C11	1.402 Å	1.385 Å
C11-C12	1.395 Å	1.386 Å
Angles		
C3-C4-C9	121.8°	122.4°
C4-C9-C10	116.0°	115.6°
C8-C9-C10	122.9°	123.1°
C9-C8-C17	122.2°	122.3°
C10-C9-C17-C18	29.4°	25.1°

* Room-temperature data. See reference [134]

structure and has D_{2h}^{18} point group symmetry at room-temperature with four molecules per unit cell [86]. The lattice constants for the orthorhombic unit cell are $|\vec{a}| = 26.901 \text{ Å}$, $|\vec{b}| = 7.187 \text{ Å}$, and $|\vec{c}| = 14.430 \text{ Å}$. Figure 4.2 shows the molecular stacking in the crystal. Most crystallites are thin or thick platelets, millimeters in lateral dimension. The face of the crystallites is the (100) plane.

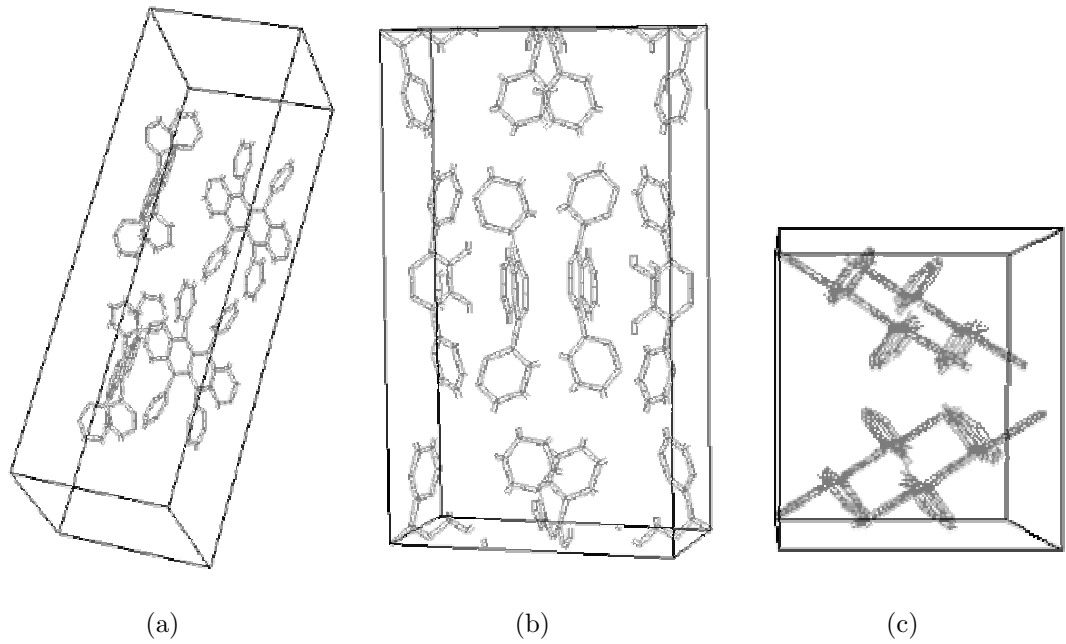


Figure 4.2: Three views of the packing in rubrene single crystals. (a) and (c) show the orientation of molecules with respect to each other while (b) is the primitive unit cell. The figures are based on x-ray data of the molecular orientation and are duplicated from reference [105].

The consensus from the literature is that the crystals have a room-temperature band gap of approximately 2.21 eV [135].

One should notice in figure 4.2 that for any rubrene molecule there exists a neighboring molecule that stands closer than any other molecules in the lattice, which is obvious from the view of figure 4.2(c). This pair may form a larger conjugated region for electron delocalization. Furthermore, the proximity of the two molecules makes the position and effects of the phenyl groups of particular interest. Recent temperature-dependent X-ray measurements observed a slight position change in the phenyl groups with respect to the backbone plane and to those on the neighboring molecule [99]. Figure 4.3 gives a picture for the packing of two nearest-neighbor molecules in the rubrene crystal at room temperature, which shows the relative position of the phenyl groups explicitly. As can be seen, the backbone planes of the two rubrene molecules are parallel to each other, separated by a distance $h = 3.74 \text{ \AA}$ in the direction perpendicular to the

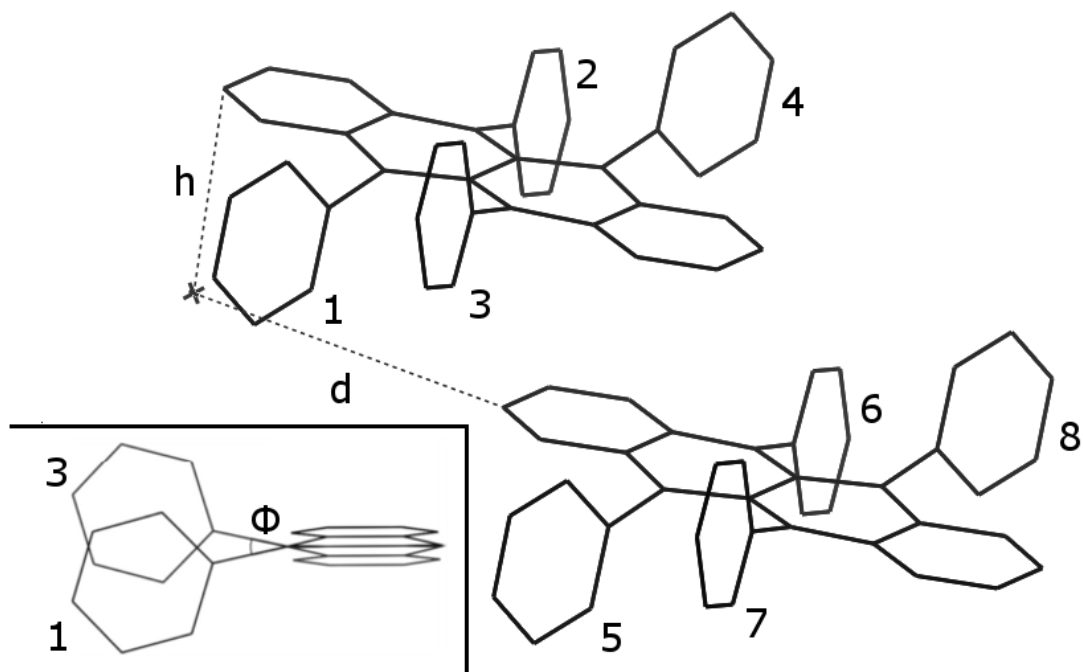


Figure 4.3: Packing of two nearest-neighbor molecules in the rubrene crystal, with the hydrogen atoms hidden; inset showing torsion angle ϕ , with the backbone perpendicular to the paper.

plane. Steric hindrance dictates that the substituted phenyl groups rotate out of the plane of the tetracene backbone, i.e., for each molecule the two phenyl groups attached to the same internal ring (taking 1 and 2 as the example) are below the backbone plane on one end, while the two phenyl groups attached to the other ring (3 and 4) are above the plane on the other end. At room temperature (293 K), the torsion angle ϕ between side groups 1 and 3 is $\sim 25^\circ$, and the molecular displacement d , which is defined as the distance between the ends of the two molecules projected on the plane of the tetracene backbone, is $\sim 6.176 \text{ \AA}$. A major feature of the rubrene crystal is that no change occurs in h with temperature [136], however both ϕ and d vary with temperature and this dependence is shown in table 4.2 and figure 4.4. It is also worthwhile to notice that phenyl groups 3 and 5 lie on opposite sides of their respective tetracene backbones to minimize the overlap between the molecules and keep the total

Table 4.2: Evolution of the phenyl group torsion angle ϕ with temperature in rubrene molecule. ϕ is defined in figure 4.3.

Temperature	ϕ^*
100 K	24.658°
125 K	24.646°
150 K	24.718°
175 K	24.744°
200 K	24.86°
235 K	24.836°
275 K	24.992°
293 K	24.996°

* Extracted from X-ray data reported in reference [99]

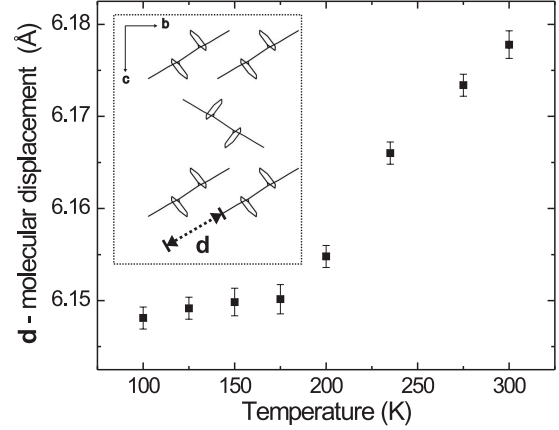


Figure 4.4: Evolution of the molecular displacement d along the long axis of the rubrene molecule with temperature. The inset represents the rubrene molecular packing viewed along the (100) direction and defines the length d of the molecular displacement. Graph is duplicated from reference [99].

energy at a minimum, and similarly for groups 4 and 6.

4.2 Raman Spectra

4.2.1 Experimental Conditions

I mounted multiple crystallites from the same growth batch at the same time as described in section 2.3, paying no deliberate attention to the orientation of the crystallites. Any polarization effects will therefore average over the entire group of crystals, which will affect analysis of the data. Studying multiple crystals also allowed me to investigate the consistency of crystals produced in a single growth run. I selected the largest crystallites from multiple growth runs in order to collect the Raman data from different points.

I recorded Raman spectra with a macro-Raman setup using a Dilor XY triple spectrometer in a backscattering configuration and a charge-coupled device (CCD) cooled with LN₂. The resolution of the spectrometer is 1 cm⁻¹. Using an Air Products closed-cycle He refrigerator in a cryogenic chamber pumped down to approximately 10⁻⁶ Torr with a diffusion pump vacuum system, I cooled the crystals to 30 K. I pumped a Spectra Physics 375B dye laser with Kiton Red dye with a Spectra-Physics 2017 Ar⁺ laser, yielding an output energy that is continuously tunable from 608 to 711 nm. I chose an excitation wavelength of 650.45 nm (1.906 eV) in the experiments to minimize the photoluminescence from the sample in order to measure the weaker Raman effect. I collected the data from approximately 25 to 1600 cm⁻¹, a range that should include both intermolecular and intramolecular vibrations. After subtracting the background, I fit all peaks using Lorentzian lineshapes with a least-squares algorithm.

As I previously mentioned, rubrene highly favors creating a peroxide layer in the presence of light and oxygen [126, 127]. I made no attempt to keep the crystals dry or in the dark, so the spectra I present here are of both the underlying bulk rubrene crystal and the surface peroxide layer. My subsequent discussion is based on the Raman data of the bulk material, which is distinguished from other interesting attributes of rubrene such as its high FET mobility (which may result from surface channel conduction).

4.2.2 Temperature Dependent Raman Results

Figure 4.5 is a representative room-temperature (300 K) Raman spectrum measured from different crystallites. Though I made no attempt to mount the crystals in specific orientations, they generated almost identical Raman spectra except for some small changes in the relative intensities of individual peaks. This confirms that the vapor deposition growth process produces very homogeneous crystals within each run. My colleague Dr. Weinberg-Wolf has conducted a detailed study of the peak positions in rubrene Raman spectra, including their

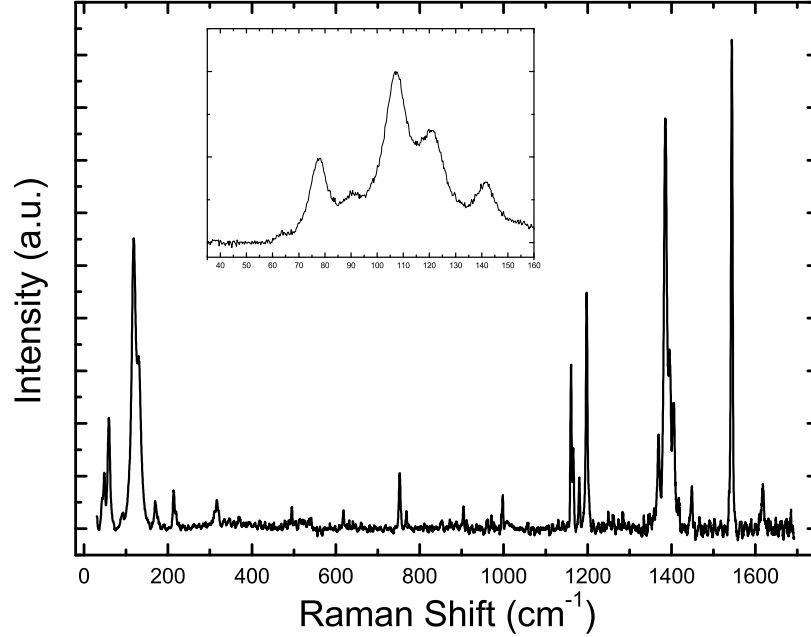


Figure 4.5: Representative room temperature (300 K) Raman spectrum of rubrene single crystals collected with an excitation energy of 650.45 nm (1.906 eV); inset showing the low-frequency range (35–160 cm^{-1}) spectrum.

general temperature dependence, comparison with calculated results and with tetracene crystals which have a similar molecular structure [105]. In contrast my study of this material focuses on the temperature dependence of its Raman spectra, especially in low-frequency range. As I mentioned above, the molecular displacement d and torsion angle ϕ change with temperature, and the effect of this change on the intermolecular vibrations can be detected by Raman measurements. Figure 4.6 is the Raman spectrum measured under low temperature (30 K), with the low-frequency peaks magnified in the inset. By comparing the insets of figures 4.5 and 4.6, one can easily see the effect of temperature on the intermolecular vibrational modes, e.g., the positions and line widths of certain low-frequency Raman peaks vary significantly, further some peaks are only observed under low-temperatures.

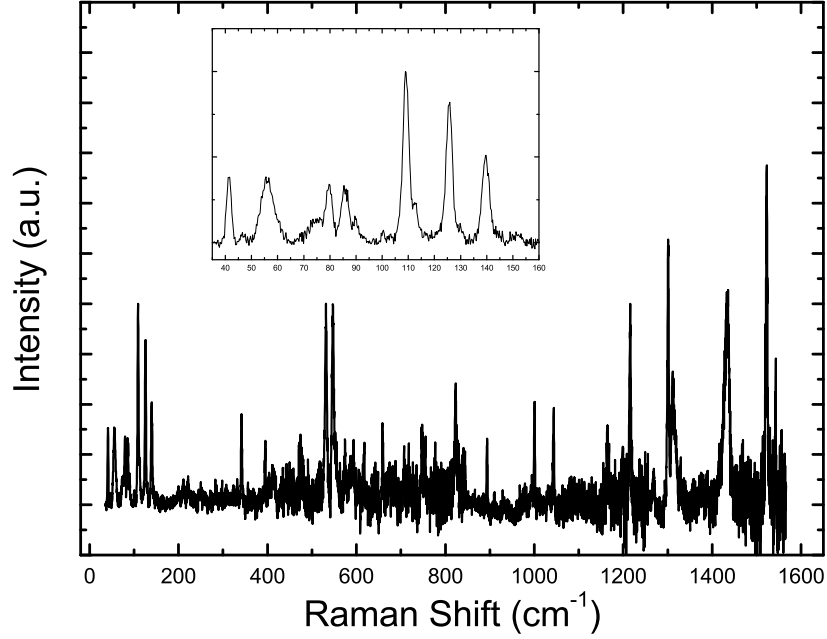


Figure 4.6: Representative low temperature (30 K) Raman spectrum of rubrene single crystals collected with an excitation energy of 650.45 nm (1.906 eV); inset showing the low-frequency range (35–160 cm^{-1}) spectrum.

These differences can be seen more clearly in figure 4.7, the low-frequency Raman spectra at low and room temperatures in the same scale, in which the peaks are labeled as No. I–VII from low to high wavenumber. One can easily tell the differences between the two spectra: peaks I and II only appear at low temperatures, and other peaks (III–VII) undergo slight shifts in position but significant broadening in line width. In order to examine the changes in peak positions and line widths with temperature more closely, I performed a series of Raman measurements under different temperatures from 30 K to 300 K, with special attention to the range of 150–200 K. After fitting all the peaks to Lorentzian lineshapes with a least-squares algorithm, I was able to determine the evolution of peak positions and line widths with temperature, which are plotted in figures 4.8 and 4.9.

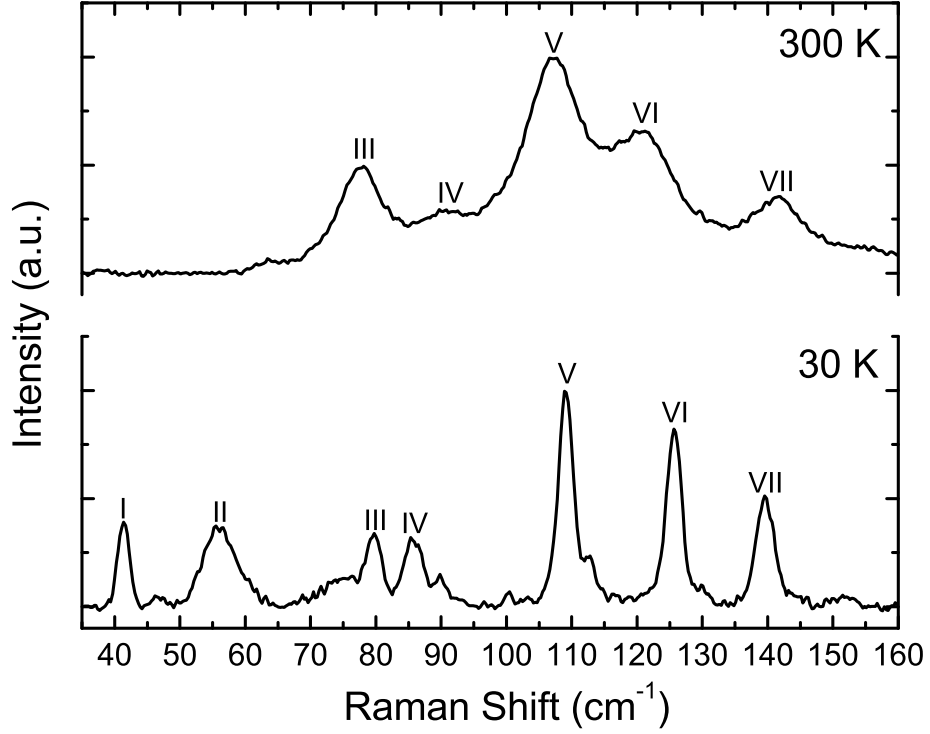


Figure 4.7: Comparison of low-frequency rubrene Raman peaks at room temperature (300 K) and low temperature (30 K).

In the upper part of figure 4.8, peaks I and II appear only at low temperatures because they red-shift to the lower frequency range quickly with increasing temperature, with little change in their line widths below ~ 80 K, above which the peaks become undetectable (below 20 cm^{-1}) with my instrument; while the lower part of the figure indicates that other peaks (III–VII) shift in position only slightly (less than 3 %). As mentioned in section 2.2.3, intermolecular modes undergo more change than do intramolecular modes with temperature due to the weaker van der Waals bonds. Peaks I and II shift in position dramatically, therefore I catalog the vibrations corresponding to peaks I and II as intermolecular vibrations. However it is not easy to ascertain what kind of vibrations correspond to peaks III–VII: firstly the simulation for an isolated rubrene molecule predicted intramolecular modes in the low-frequency region, secondly intermolec-

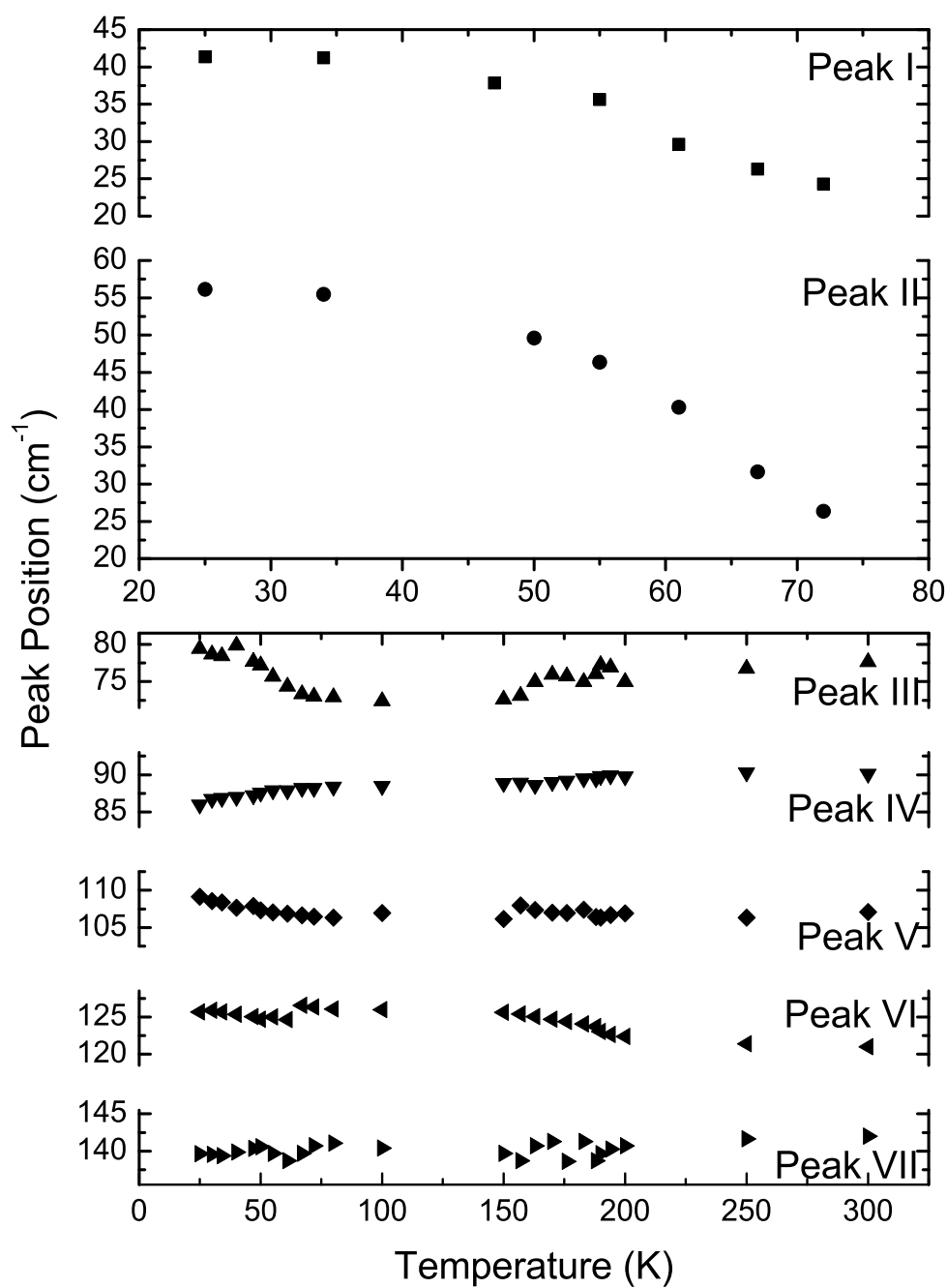


Figure 4.8: Evolution of low-frequency Raman peak positions with temperature in rubrene (note the different temperature scales in the upper and lower parts of the graph).

ular phonons with low energies should also appear below 150 cm^{-1} . I think they are neither simple intermolecular vibrations (as their positions don't shift as much as peak I and II), nor simple intramolecular vibrations (as peaks I and II prove the existence of intermolecular modes in this spectral region). Most likely I have observed in peaks III–VII strongly mixed modes of inter- and intramolecular vibrations. Venuti *et al.* studied the low-frequency phonons in rubrene by combining polarized Raman spectra with computational methods, in which they used both the rigid molecule approximation (RMA) and the flexible molecule approach (FMA) to effectively separate inter- and intramolecular vibrations and to account for the coupling between the two kinds of motions, and they came to the conclusion that there existed strong mixing between inter- and intramolecular modes below 200 cm^{-1} [100].

It is worthwhile to point out that the conclusions about low-frequency vibration modes differ somewhat from those of previous work from my lab, in which Dr. Weinberg-Wolf claimed that all the peaks below 150 cm^{-1} that she observed were intramolecular vibrations [105, 109]. To account for the reasons, firstly she didn't perform detailed temperature-dependent measurements for the low-frequency range below 80 K and as a result didn't observe the striking red-shift of peaks I and II with temperature. As a matter of fact, the intermolecular vibrations are so weak that I couldn't observe peaks I and II every time in my measurements either, and those shown in figures 4.7 and 4.8 are the best results of many trials. Secondly the isolated molecule simulation that she performed doesn't take into account the interactions between molecules (refer to section 4.1 and especially figure 4.3) and has omitted the contribution from intermolecular vibrations. In the following sections 4.3 and 4.4 I will show the important contribution of the "neighboring" rubrene molecule to the intermolecular vibrations and onsite energies.

In the upper part of figure 4.9 it is notable that only the peaks below 150 cm^{-1} (III–VII) are strongly broadened with increasing temperature. This is even more

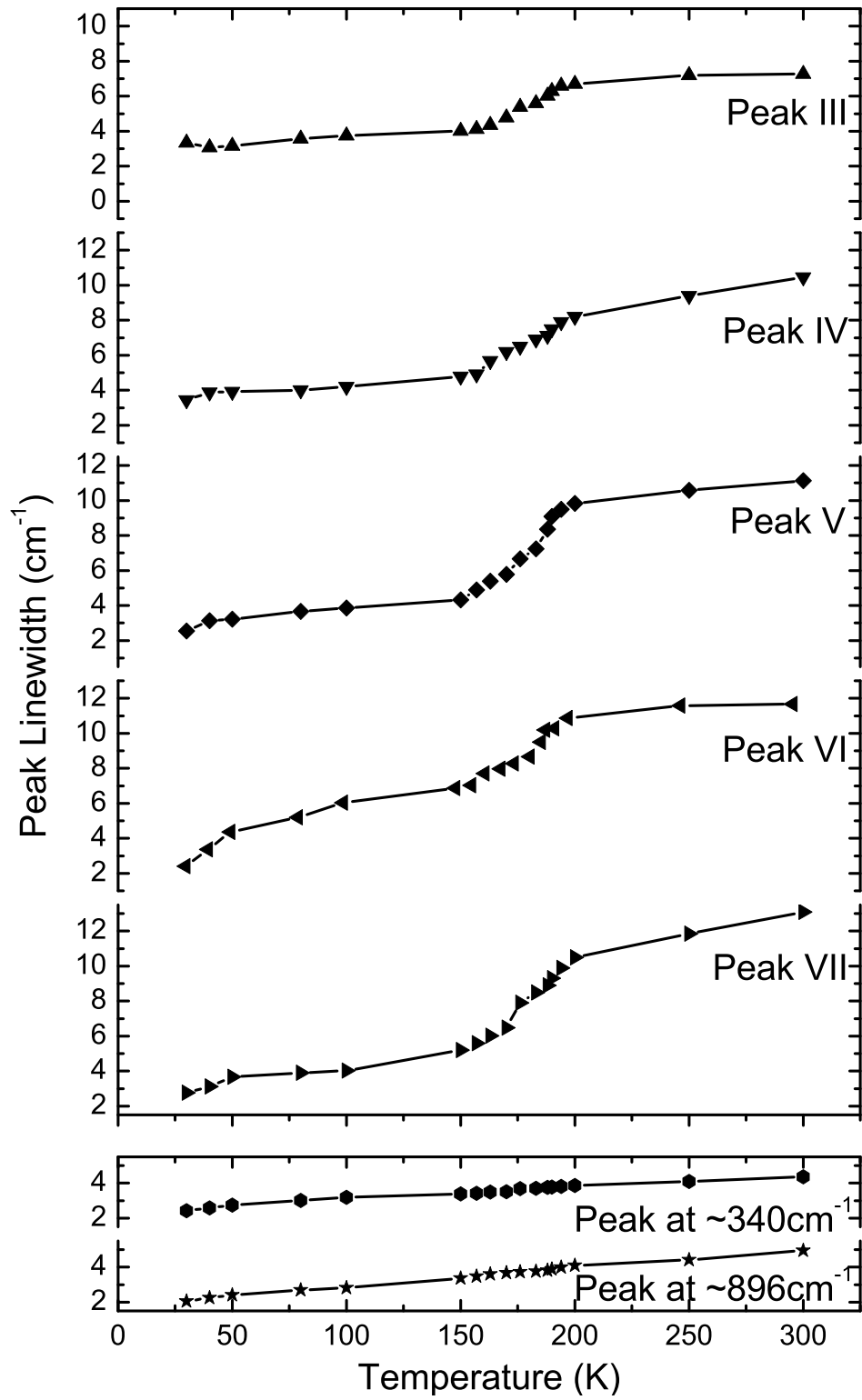


Figure 4.9: Evolution of low-frequency Raman peak line widths with temperature in rubrene; lower part being the evolution of two higher-frequency peak line widths as a comparison.

obvious if compared with the peaks at higher frequency (not shown in figure 4.8), e.g., those at $\sim 340\text{ cm}^{-1}$ and $\sim 896\text{ cm}^{-1}$ (shown in the lower part of figure 4.9), and the peaks in other materials, e.g., those in Si, Ge, and α -Sn (shown in figure 2.3(b)), the line widths of which increase only gradually. Further, around 150 K there is an abrupt change and the broadening begins to increase steeply, and at higher temperature the rate of increase slows down again. As mentioned in section 2.2.3, the spectral line width of a Raman peak is determined by the inverse of the lifetime of its corresponding phonon [137]. According to equation (2.23) increasing the temperature of a material will increase the thermal occupation number $n(\Omega)$, which means the phonons decay more easily into another state, thus a gradual peak broadening is expected in most crystals. Figure 2.3(b) has illustrated the typical gradual broadening in the simple substances Si, Ge, and α -Sn. In organic compounds with molecular structures similar to that of rubrene, such as tetracene and pentacene, this kind of gradual broadening was observed in the low-frequency range, in which the line widths increased approximately by a factor of 2 over 80–300 K [67, 138]. The low-frequency peaks in rubrene, i.e., III–VII as shown in figures 4.7 and 4.9, broaden by a factor of ~ 5 over 30–300 K, and go through an abrupt broadening at $\sim 150\text{ K}$. The broadening observed in rubrene is therefore much more dramatic than that observed in similar materials, and suggests that factors in addition to the usual phonon decay must be at work. Whether the peaks below 150 cm^{-1} result from purely intermolecular vibrations or coupled inter- and intramolecular vibrations, an abrupt change in those vibrations must occur near 150 K in order for this phenomenon to be observed in rubrene.

4.3 A New Molecular Motion Model

The massive phenyl side groups of rubrene molecules are very flexible and their motions are almost uncoupled from the backbone of the molecule [136], thus

they are responsible for the low-frequency phonons in the Raman spectra. Among these motions the one perpendicular to the backbone plane involves the smallest energy, as indicated by simulations [109] and analytical calculations [136]. It is therefore natural to conclude that the broadening of the low-frequency peaks (III–VII) is due to the shortening of the lifetime of the motion of the side groups, which results from an abrupt change of the motion perpendicular to the backbone. In this section I propose a new molecular motion model to explain the phenomenon observed in figure 4.9, and later in chapter 5 I will discuss this model in greater detail, including the potential applications in single-molecule devices as well as explanations for other phenomena observed in this material such as the changes in the mobility, thermal properties, and structure as revealed by X-ray diffraction at temperatures near ~ 150 K.

The model is illustrated in figure 4.10. Taking phenyl groups 1 and 3 as an example, in most cases they vibrate around their equilibrium positions below and above the backbone plane, respectively, and they are unable to cross the backbone plane under this circumstance, as shown in figure 4.10(a)¹. But as the temperature goes up, the probability increases that phenyl groups 1 and 3 gain enough energy to go over the energy barrier, the maximum of which occurs where they are cofacial and approach each other most closely as shown in figure 4.10(b). They then exchange sides and set up new equilibrium positions as shown in figure 4.10(c). In the actual crystal other phenyl group pairs could go through this process simultaneously, and figures 4.10(d)–4.10(f) illustrate these situations in which the additional activated pairs are 2 and 4, 6 and 8, 5 and 7, respectively.

¹The animations in the following link may be helpful for a better understanding of their motions under this circumstance [109]:
<http://www.physics.unc.edu/project/mcneil/MolecularAnimations/anim.php>.

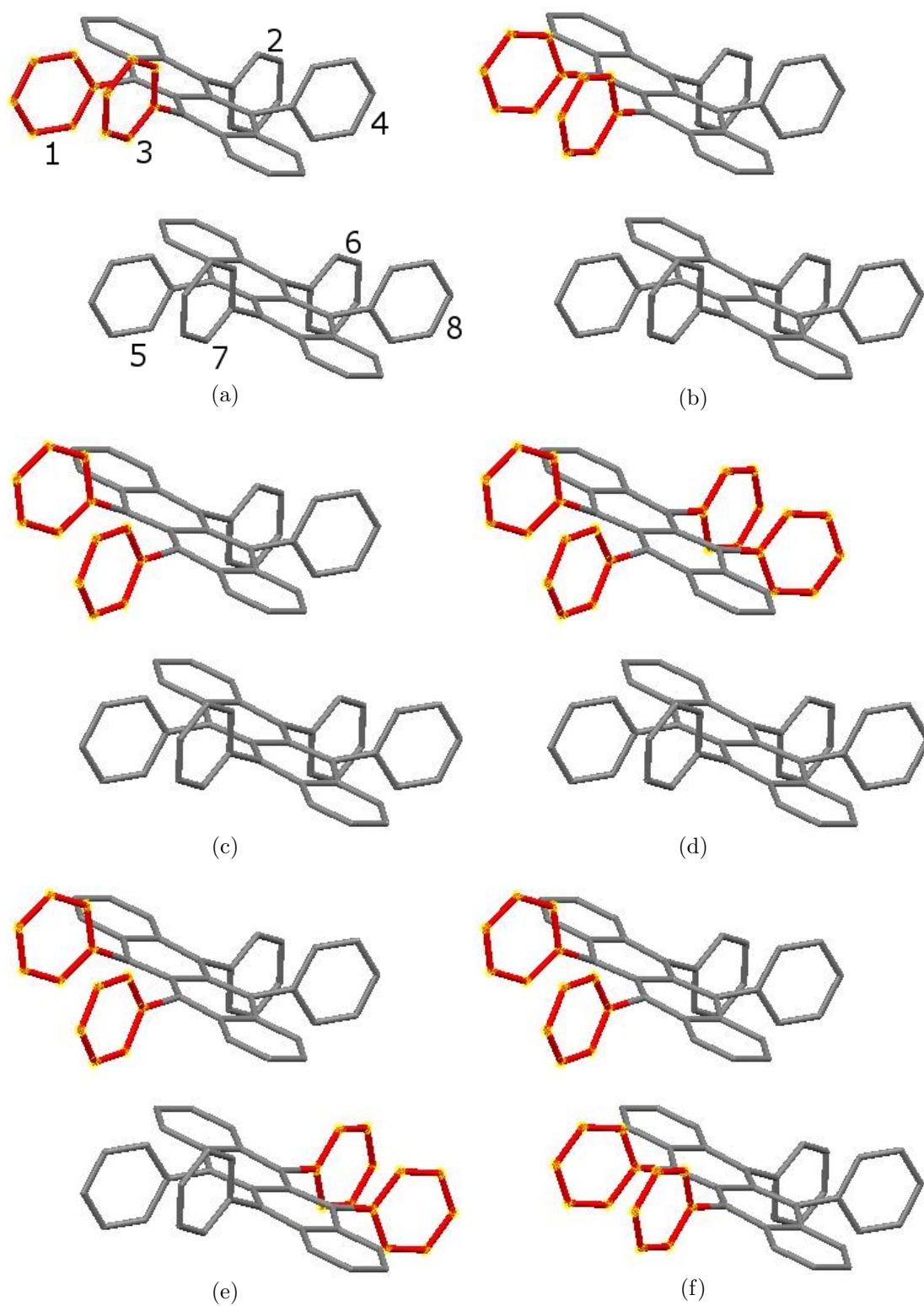


Figure 4.10: (a) Rubrene molecules in the low-energy state; (b) two phenyl groups (1 and 3) are cofacial where the maximum of the energy barrier occurs; (c) phenyl groups 1 and 3 have exchanged sides; (d)–(f) with one phenyl group pair having exchanged sides, another pair becomes cofacial simultaneously.

4.3.1 Intuitive Explanation

A particular vibration requires a particular configuration of the molecule. If the molecular configuration changes, the new configuration can no longer support the old vibration. A comparative description for a bird might be helpful to understand this statement: the bird vibrates its wings so that it can fly in the air, and this process “requires” that the two wings are symmetrically attached to the bird’s body, one on each side. One can imagine that if one of the wings suddenly “flips” beneath the bird’s body, there is no way that it can keep flying anymore, — we can say that the “flying” is terminated. A similar process happens in rubrene molecule vibrations: as the temperature goes up some of the phenyl side groups in vibrating molecules (that have been activated by incident photons) exchange sides, or “flip,” as a result the vibrational modes that are related to the side group motion in the original position are terminated, and the vibrational energies are released in the form of heat. In fact this abnormal heat flow during 150–200 K has been detected by the differential scanning calorimetry (DSC) experiment [99,139], however prior to the work described here and in reference [140] it was commonly recognized as some form of phase transition. I will discuss more about this later in section 5.2.

4.3.2 Classical Theory

The flipping effect on the Raman spectra can also be explained by classical light scattering theory. In Raman spectroscopy the cross section for scattering depends in part on the scalar product of the incident light polarization, the Raman tensor for a particular mode, and the polarization of the scattered light:

$$\frac{\partial \sigma_s}{\partial \Omega} \propto \left| \hat{\epsilon}_s \cdot \tilde{R} \cdot \hat{\epsilon}_i \right|^2 \quad (4.1)$$

The left side of equation (4.1) $\partial \sigma_s / \partial \Omega$ is the differential scattering cross section; $\hat{\epsilon}_s$ and $\hat{\epsilon}_i$ are the polarizations of the scattered and incident light, respectively;

and \tilde{R} is the Raman tensor for the system. The geometric arrangement of the experimental setup, the polarization of the incident and scattered light, and the symmetry of the crystal are therefore all important factors in the overall scattering cross section.

Rubrene is a molecular crystal, thus as an approximation we can treat the scattering from the crystal as the assembly of scattering from isolated molecules. The rubrene molecule in the low-energy state as shown in figure 4.10(a) has C_{2h} point group; with one pair of phenyl groups becoming cofacial, e.g., 1 and 3 in figure 4.10(b), it transforms to C_1 point group; after 1 and 3 have exchanged sides (figure 4.10(c)), the molecule transits to the D_2 point group. So during one simple flipping process the molecule symmetry changes twice, from C_{2h} to C_1 then to D_2 . It is worthwhile to note that if the phenyl groups on both sides of one rubrene molecule become cofacial simultaneously, e.g., 2 and 4 are cofacial with 1 and 3 already in that state, the molecule has the D_{2h} point group. However, the cofacial position occurs only for a moment during the flipping and is not a equilibrium position for the two phenyl groups. Thus no matter whether the molecule is of C_1 or D_{2h} point group at this moment, we do not need to consider it in the Raman scattering process.

So when the flipping happens the rubrene molecule symmetry changes from C_{2h} to D_2 . C_{2h} allows vibrations of four symmetry types: A_g , A_u , B_g , and A_u ; and D_2 also allows four symmetry types: A , $B_1(z)$, $B_2(y)$, and $B_3(x)$. Both point groups have centers of inversion, so only the gerade modes (those with subscript g) are Raman active. Therefore the Raman tensors for the allowed modes in C_{2h} are [141]:

$$A_g = \begin{pmatrix} a & 0 & d \\ 0 & b & 0 \\ d & 0 & c \end{pmatrix} \quad B_g = \begin{pmatrix} 0 & e & 0 \\ e & 0 & f \\ 0 & f & 0 \end{pmatrix} \quad (4.2)$$

and the Raman tensors for the allowed modes in D_2 are:

$$\begin{aligned}
A &= \begin{pmatrix} a & 0 & 0 \\ 0 & b & 0 \\ 0 & 0 & c \end{pmatrix} & B_1(z) &= \begin{pmatrix} 0 & d & 0 \\ d & 0 & 0 \\ 0 & 0 & 0 \end{pmatrix} \\
B_2(y) &= \begin{pmatrix} 0 & 0 & e \\ 0 & 0 & 0 \\ e & 0 & 0 \end{pmatrix} & B_3(x) &= \begin{pmatrix} 0 & 0 & 0 \\ 0 & 0 & f \\ 0 & f & 0 \end{pmatrix}
\end{aligned} \tag{4.3}$$

The x , y , and z in brackets after the representation indicate the direction of polarization.

The rubrene crystal cleaves along the (100) face, so the bc -plane is available in many different orientations in this experiment. In a backscattering configuration, the incident light polarization must be $\hat{\epsilon}_i = (x \ y \ 0)$ while the scattered light polarization must be $\hat{\epsilon}_s = (x' \ y' \ 0)$ where x , y , x' , and y' are components of the polarization in the plane of the crystal face. I enumerate allowed Raman modes for different point groups with backscattering geometry in tables 4.3 and 4.4. As they indicate, before the flipping one can observe both A_g and B_g modes, while after the flipping one can observe only the A mode. Again, the vibrations that belong to the B_g mode are terminated in the Raman process due to the breaking of the symmetry. Further, depending on the relative orientation of the crystal axes in the face of the crystallites and the incident polarization, the relative intensities of the A_g and B_g modes should change, and this explains why the relative intensities of individual peaks change when measurements are made on differently-oriented crystals.

4.3.3 Quantum Mechanical Theory

We can also gain some qualitative conclusions about the flipping effects by looking at the quantum mechanics expression derived in section 2.2.3. Equation (2.21) gives the broadening of the Raman line:

Table 4.3: Allowed Raman modes for C_{2h} point group with backscattering geometry.

Symmetry Type	$ \hat{\epsilon}_s \cdot \tilde{R} \cdot \hat{\epsilon}_i $
A_g	$axx' + byy'$
B_g	$e(x'y + xy')$

Table 4.4: Allowed Raman modes for D_2 point group with backscattering geometry; A_g mode being the only one that can be observed.

Symmetry Type	$ \hat{\epsilon}_s \cdot \tilde{R} \cdot \hat{\epsilon}_i $
A	$axx' + byy'$
$B_1(z)$	0^*
$B_2(y)$	0
$B_3(x)$	0

* $B_1(z)$ polarizes in z -direction and doesn't interact with light polarized in bc -plane with backscattering geometry

$$\Gamma(\vec{0}, j; \Omega) = \frac{18\pi}{\hbar^2} \sum_{\vec{q}, j_1, j_2} \left| V \begin{pmatrix} \vec{0} & \vec{q} & -\vec{q} \\ j & j_1 & j_2 \end{pmatrix} \right|^2 [n(\vec{q}, j_1) + n(-\vec{q}, j_2) + 1] \\ \times \delta(\omega(\vec{q}, j_1) + \omega(-\vec{q}, j_2) - \Omega)$$

and the matrix elements which determine the width $\Gamma(\Omega)$ are given by

$$V \begin{pmatrix} \vec{0} & \vec{q} & -\vec{q} \\ j & j_1 & j_2 \end{pmatrix} = \frac{1}{6} \left[\frac{\hbar^3}{8NM^3\omega_0\omega(q, j_1)\omega(-q, j_2)} \right]^{1/2} \\ \times \sum_{l', l''} \sum_{k, k', k''} \sum_{\alpha, \beta, \gamma} \phi_{\alpha\beta\gamma} \begin{pmatrix} 0 & l' & l'' \\ k & k' & k'' \end{pmatrix} \\ \times e_\alpha(k|\vec{0}, j) e_\beta(k'|\vec{q}, j_1) e_\gamma(k''|-\vec{q}, j_2) e^{i\vec{q}[\vec{R}(l') - \vec{R}(l'')]}]$$

where

$$\phi_{\alpha\beta\gamma} \begin{pmatrix} 0 & l' & l'' \\ k & k' & k'' \end{pmatrix}$$

is the derivative of the interatomic potential with respect to displacements along directions of the Cartesian coordinates α , β , and γ of the atoms

$$\begin{pmatrix} 0 \\ k \end{pmatrix}, \begin{pmatrix} l' \\ k' \end{pmatrix}, \begin{pmatrix} l'' \\ k'' \end{pmatrix}$$

respectively. In other words, $\phi_{\alpha\beta\gamma}$ is the force constant along three different directions. A full calculation for V before and after the flipping happens would be complex and is not attempted here. Here we simplify the interatomic potential in rubrene molecules as follows: we treat the two phenyl groups that exchanged sides as two big “atoms,” this way the potential within one rubrene molecule, i.e., that between the phenyl groups and the backbone, increases with flipped side groups (because the system energy in the configuration shown in figure 4.10(a) is at a minimum). This increases the absolute value of V and as a result the Raman line width $\Gamma(\Omega)$.

4.4 Simulations

In order to support my molecular motion model, I also calculated the onsite energies of the two-molecule units shown in figure 4.10 with different phenyl group positions and flipping angles at different temperatures using GAUSSIAN 03 [142]. I used the Hartree-Fock method for the structural optimization and the density functional theory (DFT) [143] B3LYP method [144–146] with the 6-311G(d) basis set [147,148] to calculate the energies under different conditions. All calculations started from the experimental X-ray structures provided by Dr. Jurchescu [99], and ran on an SGI Origin 3800 with 64 CPUs and 128 GB memory running the IRIX 6.5 OS.

Defining the energy differences between figures 4.10(a) and 4.10(b), 4.10(a) and 4.10(d), 4.10(a) and 4.10(e), 4.10(a) and 4.10(f) as ΔE_1 , ΔE_2 , ΔE_3 , and ΔE_4 , respectively, I calculated the energies that are needed to change the phenyl group positions at different temperatures and present the result in figure 4.11. I can make several statements based on the energy difference curves revealed in

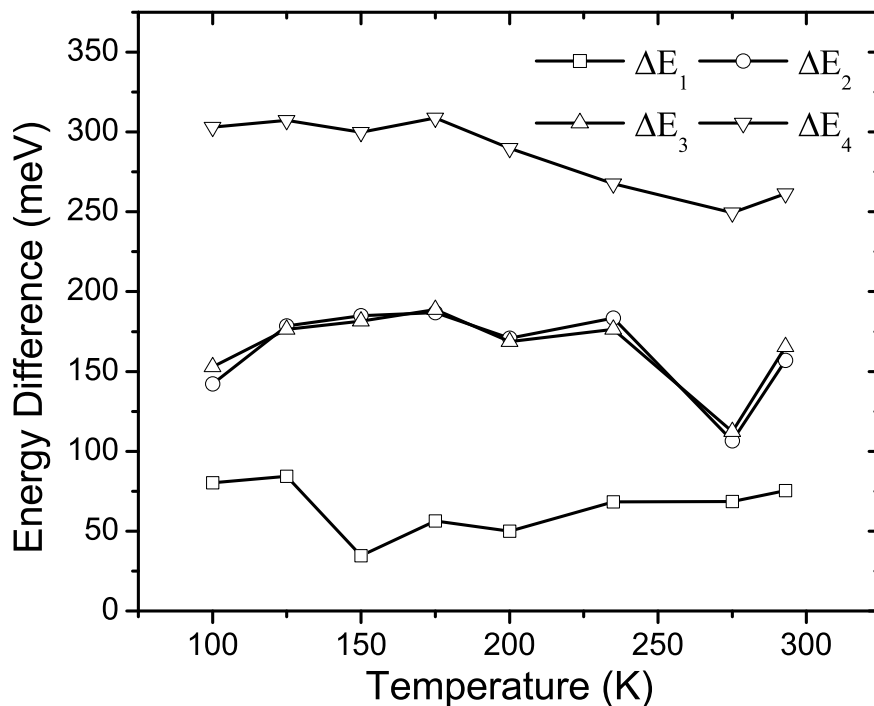


Figure 4.11: Evolution of energy differences between different phenyl group positions with temperature.

figure 4.11. First of all the relation $\Delta E_1 < \Delta E_2 \approx \Delta E_3 < \Delta E_4$ is reasonable, because the activation of an additional pair of phenyl groups requires additional energy; and ΔE_4 is remarkably larger than the other three because phenyl groups 3 and 5 become very close with the 1-3 and 5-7 pairs activated simultaneously. Secondly the curves for ΔE_2 and ΔE_3 are almost coincident, because the phenyl side groups are very flexible and their motions are almost uncoupled from the backbone and from those on the other side of the same molecule as well as on

the neighboring molecule. Thirdly in our model the ΔE 's are affected by two factors: within the molecule by the torsion angle ϕ between the phenyl groups that exchange sides, and externally by the molecular displacement d between the molecules. Generally speaking, larger displacement and smaller torsion angle lead to smaller ΔE 's. However, the larger torsion angle generates more overlap with, and thus repulsion of, the phenyl groups on the neighboring molecule, in which case the two molecules displace slightly with respect to each other, increasing d to keep the system energy low. Thus larger torsion angle induces a larger displacement, and the two effects compete to affect the ΔE 's. That is why although the molecular displacement increases monotonically with increasing temperature (refer to figure 4.4) [99], the energy differences do not. Fourthly it is noteworthy that the torsion angle between the two phenyl groups after they have exchanged sides is smaller than in the original position; our calculation shows it to be less than $\sim 10^\circ$ (in figure 4.10 I used larger torsion angles to make the change more obvious). Thus the structure in which the phenyl groups have exchanged sides, as shown in figure 4.10(c), is unstable, and goes back to figure 4.10(a) easily.

Specifically the transition rate $1/\tau$ for the phenyl groups to cross the energy barrier is

$$\frac{1}{\tau} = \nu e^{-\frac{\Delta E}{k_B T}} \quad (4.4)$$

where $\nu \sim 10^{12}$ Hz is the typical vibration frequency and ΔE is the energy barrier in the different cases. Employing the calculated ΔE 's, I am able to explain in detail my Raman observations. From 30–150 K $1/\tau$ increases with temperature with a relatively large but constant ΔE_1 (since d changes only slightly); around 150 K there is a sudden decrease of the energy barrier, which increases $1/\tau$ exponentially, enabling more phenyl groups to exchange sides and enlarging the line widths as shown in figure 4.9. Above 150 K ΔE_1 remains at a relatively small

value, but increases with temperature on average, which slows down the flipping rate. Meanwhile the increase in the number of molecules with flipped phenyl groups prevents an additional flip in the neighboring molecules (as shown in figure 4.10(d)–4.10(f)), since the energies needed to do so (ΔE_{2-4}) are significantly larger, as seen in figure 4.11. Such large energy barriers further slow down the flipping rate, therefore at higher temperature this effect becomes weak and the Raman peak broadening slows down.

4.5 Conclusion

Since rubrene is of interest to many researchers for its possible application in devices due to its extremely high hole mobility, a fundamental understanding of the underlying physics that makes the material unique is important. The temperature-dependent Raman data indicate that in the spectral region below 150 cm^{-1} the two phonons with the lowest frequency red-shift with increasing temperature rapidly, while other peaks shift little in position but broaden significantly in line width especially in the 150–200 K range. I catalog the two phonons with lowest frequency as intermolecular modes, and other five peaks as the strong coupling of inter- and intramolecular vibrations. I construct a new model to describe the phenyl groups’ motion under different temperatures, in which the Raman peaks’ broadening results from disorder as the phenyl groups exchange sides of the backbone plane and break the symmetry. I also simulated the energies of different phenyl groups’ motion to support the theory.

Chapter 5

Impacts of Our Molecular Motion Model

I proposed a new model in section 4.3 to describe changes in the molecular motion in crystalline rubrene as the temperature changes and discussed how the DFT simulations were used to support the theory and further explain the phenomena observed in temperature-dependent Raman measurements in section 4.4. In this chapter I will further discuss implications of this model for other properties and applications of the material, such as the temperature dependence of its charge transport, structural and calorimetric observation of changes near 150 K, and potential application in single-molecule device design.

5.1 Mobility

I mentioned in section 1.2 the abnormal temperature dependence of the carrier mobility in rubrene single crystals. In figure 1.4, the mobility increases rapidly from low temperature to ~ 150 – 175 K, above which it decreases gradually as the temperature increases further. This temperature dependence of the mobility is markedly distinguished from that in tetracene and pentacene, and the theories and models used to explain the mobility-temperature relations in tetracene and

pentacene fail to explain the behavior in rubrene [99, 100]. Although some have suggested possible reasons for the mobility drop below 140 K, such as shallow traps [5, 92] or enhancement of the effective mass of quasiparticles in molecular orbital bands [101], it has remained as an important unsolved problem in rubrene.

Let's consider band transport and hopping transport, the two fundamental transport mechanisms in organic semiconductors. In the hopping model, the rate of charge transfer (W) between neighboring molecules can be described as follows according to Marcus theory [149, 150],

$$W = \frac{2t_{mn}^2}{h} \left(\frac{\pi^3}{\lambda k_B T} \right)^{\frac{1}{2}} \exp \left(-\frac{\lambda}{4k_B T} \right) \quad (5.1)$$

where t_{mn} is the electronic coupling integral for all the molecular pairs, with m and n denoting the nearest-neighbor molecules, and λ is the sum of inter- and intramolecular reorganization energy for the charge carriers. The mobility μ can be directly calculated from W by the Nernst-Einstein relation through the diffusion coefficient D [151, 152],

$$D = \frac{1}{2s} \sum_i r_i^2 W_i^2 \quad (5.2)$$

and

$$\mu = \frac{e}{k_B T} D \quad (5.3)$$

where s is the dimensionality of the crystal, r is the distance between the pairs of molecules, and W_i is the probability for the charge carrier to hop to a particular i th neighbor, normalized over the total hopping rate ($\sum_i W_i$). Equations 5.1–5.3 clearly suggest that smaller λ , larger t and higher T lead to larger μ . On the other hand, in band transport with the interaction of the delocalized carriers with the phonons (the main scattering process), the carrier mobility in crystals decreases with temperature according to the following equation,

$$\mu = CT^{-n} \quad (5.4)$$

where C and n are constants [153].

These two effects are in competition to affect carrier mobility. In rubrene, the electronic coupling is strong thus the hopping transport takes the leading role at low temperature. Plus, a large fraction ($\sim 25\%$) of the intramolecular reorganization energy comes from the low-frequency vibrational modes, i.e., the motion of the phenyl side groups, as indicated by calculations at the DFT level [136]. Therefore when the phenyl group flipping eliminates these vibrations, λ is reduced accordingly.

With this model it is possible to explain the behavior of the carrier mobility of rubrene single crystals. At low temperature, T changes the flipping rate exponentially, and as more low-frequency vibrational modes are eliminated, λ is reduced and the hopping process becomes easier, which explains why the carrier mobility increases with temperature below 150 K. As the temperature increases, the second effect (phonon scattering) begins to dominate for charge transport. But more and more phenyl groups are activated to exchange sides in the range 150–200 K, and they enhance the hopping between neighboring molecules, so μ remains nearly constant. At higher temperature, the number of flipped phenyl group pairs no longer increases significantly, as discussed above, and with band transport becoming dominant, the mobility decreases gradually with temperature. One can refer to figure 1.4 for the carrier mobility behavior in rubrene over this temperature range.

Notably, in equation 5.1 λ appears in the exponential position, and as a result μ could fluctuate greatly with even a tiny change in λ in hopping transport, especially at low temperatures. For example, with the assumption that the electronic coupling integral t and the distance between molecule pairs r fixed, a 1% decrease in λ causes a $\sim 14\%$ increase in μ at 150 K. Therefore in the real situation, an increase of μ by a factor of 2–3 in the range 125–175 K, as shown in figure 1.4,

is possible even in the presence of trapping. A measurement of Hall mobility in the range 100–175 K, which is independent of trapping and yields the change of free-carrier mobility with increasing temperature, would clarify the picture. We also notice that in the range 230–290 K, the Hall mobility at fixed gate voltage changes only slightly with temperature [96], which agrees with our model.

It should be noted that this model of the relationship between the motion of the phenyl side groups and the temperature dependence of the mobility does not of itself explain the unusually large mobility observed in this material. Recent work has pointed to oxidation on the crystal surface as being an important contributor to the high mobility measured in FET structures (in which the conduction is limited to a narrow channel close to the rubrene surface) [154–156]. However, the phenomenon of the flipping of the phenyl groups should occur throughout both the bulk and the surface of the crystal, and therefore will influence the temperature dependence of the charge transport regardless of where the transport takes place.

5.2 Thermal, Structural and Other Properties

Other phenomena observed in rubrene single crystals are manifest in the results of differential scanning calorimetry (DSC) and X-ray diffraction measurements. DSC measurements showed a small bump over 155–195 K which is centered at 173 K, as shown in figure 5.1. This abnormality, together with the mobility behavior near 175 K, were taken as evidence for a structural phase transition in rubrene. However, no such transition was observed by X-ray diffraction [99] and polarized Raman scattering [100]: X-ray diffraction confirmed the crystal structure was orthorhombic over the entire temperature range from 100 K to 293 K, and the lattice parameter only changed slightly and linearly with temperature; and room-temperature polarized Raman measurements on various surfaces of the crystal observed no multi-phase coexistence.

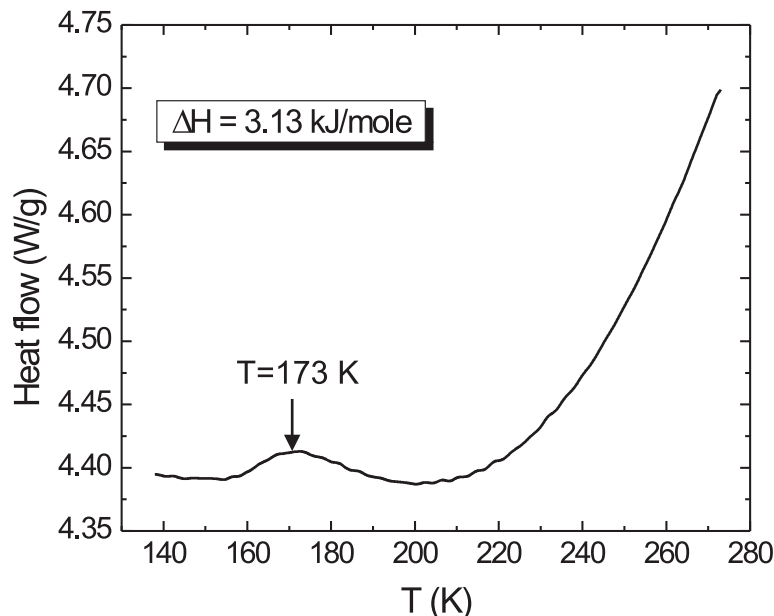


Figure 5.1: Differential scanning calorimetry (DSC) of crushed rubrene single crystals carried out in N_2 atmosphere, which shows a small bump centered at 173 K. The graph is duplicated from reference [139].

The discrepancy among conclusions as indicated by different measurements can be explained by our molecular motion model, in which the effects of phenyl groups flipping depend on temperature. In the temperature range of 150–200 K significantly more phonons are eliminated due to the flipping effect, as discussed in section 4.4 and as can be seen in figure 4.9. This is a moderately exothermic process but not a full phase transition. On the other hand, the phenyl groups exchange sides back and forth at a very high frequency (typically $\sim 10^{12}$ Hz) while the backbones basically stay still, a process too rapid to be captured in conventional X-ray diffraction.

One interesting result that is derived from the X-ray diffraction experiment is that the molecular displacement d increases with temperature and the rate begins to accelerate from ~ 170 K (see figure 4.4). The reason for this is similar to the reason why a larger torsion angle induces a larger displacement as discussed in section 4.4: the flipped phenyl groups generate overlap with, and thus repulsion of, the neighboring molecule. Therefore d increases to keep the system energy

low. The displacement change then affects the further flipping through the energy barriers, as discussed also in section 4.4.

In addition to the experiments that have already been performed at different temperatures, our model has several important implications for future NMR and X-ray studies as well. Above 150 K phenyl groups that exchange sides at rates exceeding the chemical shift anisotropy will experience motional narrowing and would be easily distinguished from the stationary backbone spectrum. In addition, a detailed examination of the Debye-Waller factor around 150 K would clarify how the flipping-induced disorder affects the X-ray diffraction pattern.

Further, although below room temperature the flipping is an intermittent phenomenon, there could exist a higher temperature above which the phenyl groups could exchange sides back and forth freely. My calculation shows that the energy barrier ΔE_1 for one phenyl group pair in an isolated rubrene molecule is ~ 80 meV, based on which I estimate the “temperature for free flipping” T_f to be ~ 900 K. This is much higher than the melting point of the rubrene single crystal (~ 590 K), and the hypothesis is therefore difficult to verify directly. However, as the temperature goes up precursors of this “free flipping” transition might be observed in the above-mentioned measurements, e.g., a sudden narrowing of the NMR peaks, or an abnormal attenuation of X-ray scattering.

A similar effect might also be observable in other materials whose molecules have massive but flexible side groups and are loosely bound to each other. For example, consider 5,12-Bis(4-*tert*-butylphenyl)-6,11-diphenylnaphthacene (5,12-BTBR), a rubrene derivative with three additional CH_3 groups on two of the side phenyl groups, the molecular and lattice structures of which can be found in figure 5.2. As can be seen, 5,12-BTBR has the side phenyl groups above and below the backbone plane, and the molecule packing is similar to that in rubrene. The mobility in this material has been found to be as high as $12 \text{ cm}^2/\text{Vs}$ in the single-crystal FET structure [158], which is comparable to that in rubrene. Therefore 5,12-BTBR can be a good example for a parallel study with rubrene.

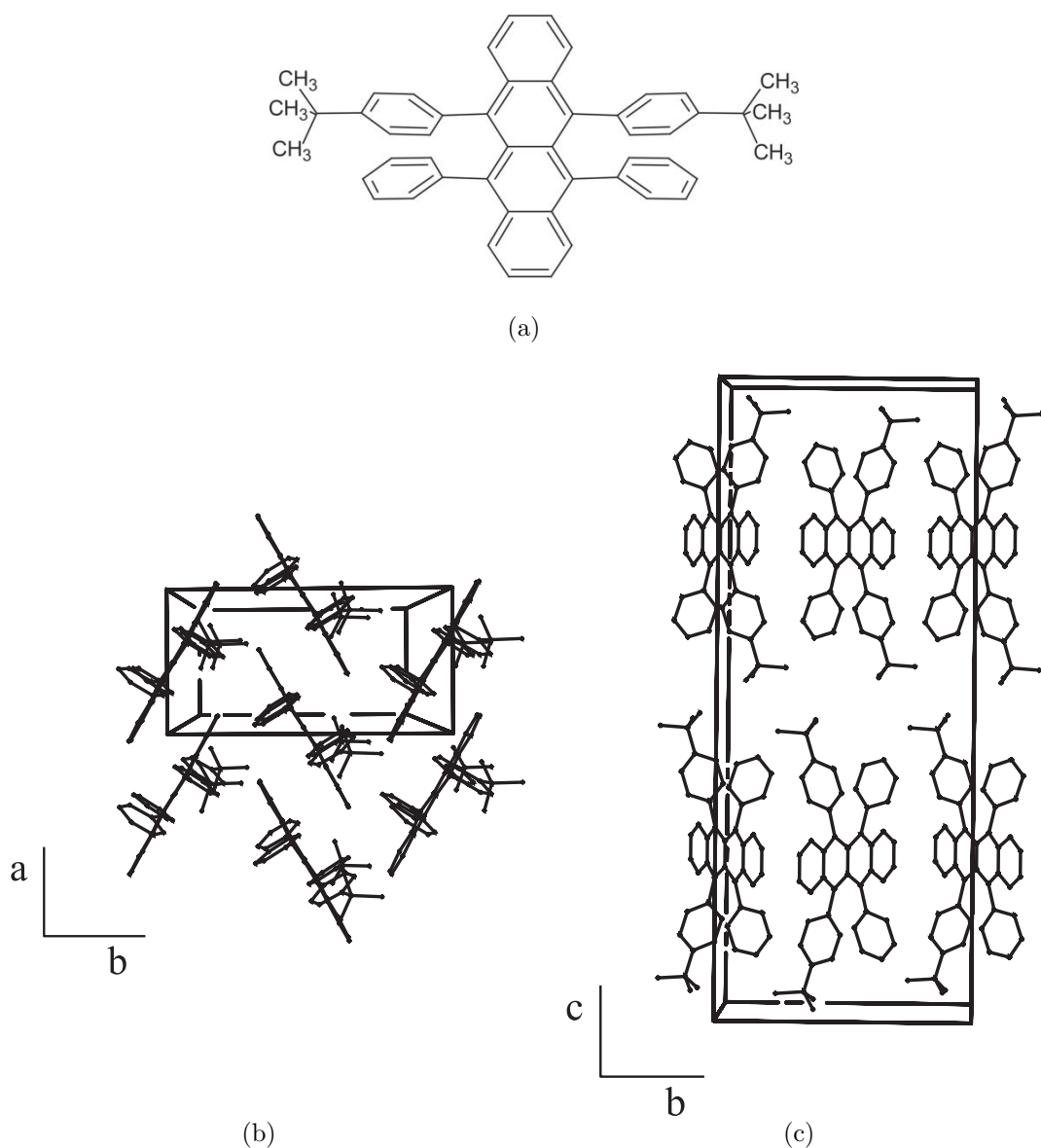


Figure 5.2: (a) Molecular structure for the rubrene derivative 5,12-BTBR; (b) and (c) lattice structure perspective view for 5,12-BTBR along different axes, showing the molecule packing is similar to that in rubrene. Drawings are duplicated from references [157, 158].

5.3 Application in Single-Molecule Devices

Transistors are the fundamental devices in integrated circuits. As efforts have been made to produce ever-smaller devices, people have pushed the limit to single-molecule transistors, the conduction channels of which are defined by

a single molecule. The solid-state molecular transistors that have already been made are based on three mechanisms: Coulomb blockade, in which the flow of electrons is controlled by the sequential charging of a molecule; the Kondo effect, in which conducting electrons interact with local spin (intrinsic angular momentum) in a molecular junction [25–28]; and the electrostatic modulation of the molecular-orbital energy of a single molecule, the approach of which was predicted in 2004 [29] and realized recently [30].

The model that I proposed describes an intrinsic property of rubrene molecules, and is applicable for molecular crystals as well as an isolated molecule, therefore it also regulates the properties of the molecule that can be used in a rubrene-based single-molecule transistor.

One can imagine that in a transistor with the source and drain electrodes in contact with the two ends of the backbone of a rubrene molecule, the vibrational excitation of the rubrene molecule could be coupled to an electron tunnelling on and off the molecule. These vibrational modes would be present irrespective of the charge state of the molecule. In the temperature range of 150–200 K, these tunnelling pathways would shut down as the vibrations that excite the transport terminate due to the flipping effect. The conduction in transistors of this kind would stay constant from low temperature to ~ 150 K, decrease rapidly from 150–200 K, and once again stay constant at higher temperatures.

One can also imagine another “conformational” transistor with the source and drain electrodes in contact with the phenyl groups on one side of the rubrene molecule. Taking figure 4.3 inset as a reference, the source would be in contact with phenyl group 1 below the backbone and inside the paper plane, while the drain would be in contact with phenyl group 3 above the backbone and outside the paper plane, so that neither 1 nor 3 would touch the opposite electrode even after the flip happens. In the temperature range of 150–200 K, the flipping effect could cut off the current by tilting the phenyl groups 1 and 3 away from a contact. The conduction in transistors of this kind would follow a similar

temperature dependence trend as the above one.

The statements that I make here are preliminary ideas for the possible application of our molecular motion model in single-molecule device design. Much work still needs to be done to make a working transistor that can be used to verify the hypotheses, e.g., making the rubrene molecule backbone ends or the specific phenyl groups come in contact with the source and drain electrodes is a challenging task. However, I hope that the predictions and inferences that I made here are inspiring for future research on organic molecules for various applications.

5.4 Conclusion

Properties of rubrene single crystals observed by other research groups are consistent with the inferences of the model that I proposed and explained in the previous chapter. I discussed how the flipping effect changes the mobility in the temperature range 150–200 K by reducing the reorganization energy, thus making the carrier hopping easier in the rubrene single crystal. Other phenomena explained by the model are DSC and X-ray measurements: the DSC measurement showed a smooth bump over 155–195 K because in this range significantly more phonons were eliminated by the flipping effect and the vibrational energy was released in form of heat; meanwhile the phenyl groups flip back and forth rapidly while the backbone stays still, so that traditional X-ray measurements cannot capture the structural change. As more and more phenyl groups exchange sides, the two closest rubrene molecules slide along the backbone plane in opposite direction, increasing molecular displacement d to reduce the system energy.

Starting from the model I also predicted possible temperature-dependent NMR and X-ray properties of rubrene, and discussed potential applications in manufacturing single-molecule transistors. The flipping effect could affect other crystals with a similar molecular structure, e.g., 5,12-BTBR.

Chapter 6

Conclusions

In this dissertation, I have tried to build a connection between the molecular vibrations and the electronic properties of some organic semiconducting molecular crystals. The desire to produce efficient light-emitting devices and field-effect transistors drives the current interest in the properties of these molecular crystals. Current technologies in organic chemistry make the customization of molecules with the desired optical properties. Therefore a good understanding of the structures and properties of materials is desirable, as once such a connection is established it will be possible to tailor the molecules to fulfill the requirements for device performance.

Oligoacenes and their derivatives have an important role in fundamental physics research, because their molecules are relatively small and simple and their molecular structures have many similarities that can be informative in a parallel study. One oligoacene derivative, rubrene, has been found to have high mobility and can be used to fabricate a variety of devices. However, the origin of such an unusually high mobility and its temperature dependence were not clear prior to this study.

I therefore have focused on three simple oligoacenes and two oligoacene derivatives that have drawn considerable attention from other researchers for their possible applications in a host of devices. A complete understanding of the rela-

tionship between structure and electronic properties is still a goal for the distant future, but this work has started to illustrate some of the interesting connections in these materials.

In the parallel study of anthracene, tetracene, and pentacene Raman spectra I identify several vibrational modes in the low-frequency range in each material. I have cataloged most of them as intermolecular interactions in the three oligoacene single crystals, because they are not predicted by the DFT calculations of one isolated molecule. However I have observed that the coupling strengths decrease as the number of benzene rings increase. The DPA molecule is larger than those of the oligoacenes, and the side phenyl groups prevent close packing. Although the intermolecular interactions are even weaker in DPA than in the simple oligoacenes, I am still able to observe them in the low-frequency range.

In the temperature-dependent Raman spectra of rubrene I have observed that the two phonons with the lowest frequency red-shift with increasing temperature rapidly, while other peaks shift little in position but broaden significantly in line width especially in the 150–200 K range. I catalog the two phonons with lowest frequency as intermolecular modes, and five other low-frequency peaks as the strong coupling of inter- and intramolecular vibrations. I have constructed a new model to describe the phenyl group motion, in which the phenyl groups exchange sides of the backbone plane and break the symmetry as the temperature increases. This flipping effect induces disorder and eliminates the phonons that involve the motion of phenyl groups, and therefore broadens the line widths in the Raman spectra. I have also calculated the energies of different phenyl group motions to support the theory. I have further discussed how the flipping effect changes the mobility in the temperature range 150–200 K by reducing the reorganization energy, thus making the carrier hopping easier. Other phenomena observed in this material also support the model, e.g., the DSC measurement has captured the heat in 155–195 K that is transformed from the molecular vibrations, and the X-ray measurement has observed that the molecular displacement d increases to

keep the system energy at low as the phenyl groups exchange sides.

Oligoacenes and their derivatives, including anthracene, tetracene, pentacene, and DPA, rubrene, are promising molecular crystals, the thin films of which have been incorporated into variety of devices. The studies that I have reported in this dissertation, the effects of molecular vibration on the material's charge transport properties, contribute not only to a fundamental understanding of the interplay between the structure and electronic properties, but also to the potential application of the material in manufacturing single-molecule devices. Once scientists reach the ultimate goal of understanding how to tailor molecules to have the exact properties required for specific applications, people can create innovative devices with high efficiency, higher resolution, and longer lifetime at the molecule level, which will better serve people and the world's needs.

REFERENCES

- [1] M. Pope and C. E. Swenberg, *Electronic Processes in Organic Crystals and Polymers* (Oxford University Press, New York, 1999).
- [2] C. W. Tang and S. A. VanSlyke, "Organic electroluminescent diodes," *Applied Physics Letters* **51**, 913–915 (1987).
- [3] G. Horowitz, F. Garnier, A. Yassar, R. Hajlaoui, and F. Kouki, "Field-effect transistor made with a sexithiophene single crystal," *Advanced Materials* **8**, 52–54 (1996).
- [4] G. Horowitz, "Organic thin film transistors: From theory to real devices," *Journal of Materials Research* **19**, 1946–1962 (2004).
- [5] R. W. I. de Boer, M. E. Gershenson, A. F. Morpurgo, and V. Podzorov, "Organic single-crystal field-effect transistors," *Physica Status Solidi a - Applied Research* **201**, 1302–1331 (2004).
- [6] C. Reese and Z. N. Bao, "Organic single-crystal field-effect transistors," *Materials Today* **10**, 20–27 (2007).
- [7] G. Horowitz, "Organic semiconductors for new electronic devices," *Advanced Materials* **2**, 287–292 (1990).
- [8] H. Inokuchi, "Organic semiconductors: Past and present," *Molecular Crystals and Liquid Crystals* **125**, 51–58 (1985).
- [9] V. Podzorov, V. M. Pudalov, and M. E. Gershenson, "Field-effect transistors on rubrene single crystals with parylene gate insulator," *Applied Physics Letters* **82**, 1739–1741 (2003).
- [10] A. R. Brown, C. P. Jarrett, D. M. de Leeuw, and M. Matters, "Field-effect transistors made from solution-processed organic semiconductors," *Synthetic Metals* **88**, 37–55 (1997).
- [11] G. Horowitz, "Organic field-effect transistors," *Advanced Materials* **10**, 365–377 (1998).
- [12] F. Garnier, "Thin film transistors based on organic conjugated semiconductors," *Current Opinion In Solid State & Materials Science* **2**, 455–461 (1997).

- [13] H. E. Katz, "Organic molecular solids as thin film transistor semiconductors," *Journal of Materials Chemistry* **7**, 369–376 (1997).
- [14] D. J. Gundlach, Y. Y. Lin, T. N. Jackson, S. F. Nelson, and D. G. Schlom, "Pentacene organic thin-film transistors - Molecular ordering and mobility," *IEEE Electron Device Letters* **18**, 87–89 (1997).
- [15] D. J. Gundlach, J. A. Nichols, L. Zhou, and T. N. Jackson, "Thin-film transistors based on well-ordered thermally evaporated naphthacene films," *Applied Physics Letters* **80**, 2925–2927 (2002).
- [16] M. Matsumura and T. Furukawa, "Properties of organic light-emitting devices with a rubrene sub-monolayer inserted between electron- and hole-transport layers," *Japanese Journal of Applied Physics Part 1 - Regular Papers Short Notes & Review Papers* **41**, 2742–2745 (2002).
- [17] J. R. Sheats, H. Antoniadis, M. Hueschen, W. Leonard, J. Miller, R. Moon, D. Roitman, and A. Stocking, "Organic electroluminescent devices," *Science* **273**, 884–888 (1996).
- [18] Z. L. Zhang, X. Y. Jiang, and S. H. Xu, "Energy transfer and white emitting organic thin film electroluminescence," *Thin Solid Films* **363**, 61–63 (2000).
- [19] H. Aziz and Z. D. Popovic, "Study of organic light emitting devices with a 5,6,11,12-tetraphenylnaphthacene (rubrene)-doped hole transport layer," *Applied Physics Letters* **80**, 2180–2182 (2002).
- [20] J. Ackermann, C. Videlot, and A. El Kassmi, "Growth of organic semiconductors for hybrid solar cell application," *Thin Solid Films* **403**, 157–161 (2002).
- [21] T. Fromherz, F. Padinger, D. Gebeyehu, C. Brabec, J. C. Hummelen, and N. S. Sariciftci, "Comparison of photovoltaic devices containing various blends of polymer and fullerene derivatives," *Solar Energy Materials and Solar Cells* **63**, 61–68 (2000).
- [22] A. S. Arutyunov, "Rubrene-based film actinometer for ultraviolet-radiation," *Instruments and Experimental Techniques* **25**, 769–771 (1982).
- [23] B. Crone, A. Dodabalapur, A. Gelperin, L. Torsi, H. E. Katz, A. J. Lovinger, and Z. Bao, "Electronic sensing of vapors with organic transistors," *Applied Physics Letters* **78**, 2229–2231 (2001).
- [24] L. Wang, D. Fine, and A. Dodabalapur, "Nanoscale chemical sensor based on organic thin-film transistors," *Applied Physics Letters* **85**, 6386–6388 (2004).

- [25] J. Park, A. N. Pasupathy, J. I. Goldsmith, C. Chang, Y. Yaish, J. R. Petta, M. Rinkoski, J. P. Sethna, H. D. Abruna, P. L. McEuen, and D. C. Ralph, “Coulomb blockade and the Kondo effect in single-atom transistors,” *Nature* **417**, 722–725 (2002).
- [26] W. J. Liang, M. P. Shores, M. Bockrath, J. R. Long, and H. Park, “Kondo resonance in a single-molecule transistor,” *Nature* **417**, 725–729 (2002).
- [27] S. Kubatkin, A. Danilov, M. Hjort, J. Cornil, J. L. Bredas, N. Stuhr-Hansen, P. Hedegard, and T. Bjornholm, “Single-electron transistor of a single organic molecule with access to several redox states,” *Nature* **425**, 698–701 (2003).
- [28] L. H. Yu and D. Natelson, “The Kondo effect in C-60 single-molecule transistors,” *Nano Letters* **4**, 79–83 (2004).
- [29] A. W. Ghosh, T. Rakshit, and S. Datta, “Gating of a molecular transistor: Electrostatic and conformational,” *Nano Letters* **4**, 565–568 (2004).
- [30] H. Song, Y. Kim, Y. H. Jang, H. Jeong, M. A. Reed, and T. Lee, “Observation of molecular orbital gating,” *Nature* **462**, 1039–1043 (2009).
- [31] V. A. Lisovenko, G. A. Sandul, and M. T. Shpak, “Nature of the background In Raman-scattering spectra of anthracene single-crystals,” *Optika I Spektroskopiya* **64**, 360–365 (1988).
- [32] V. I. Broude, A. A. Maksimov, and I. I. Tartakovskii, “Resonant Raman-scattering of light In anthracene-crystals,” *Jetp Letters* **27**, 397–399 (1978).
- [33] A. A. Maksimov and I. I. Tartakovskii, “Stimulated resonant Raman-scattering of light In anthracene-crystals,” *Physica Status Solidi B - basic Research* **107**, 55–60 (1981).
- [34] J. Rasanen, F. Stenman, and Penttine.E, “Raman-scattering from molecular-crystals. 2. Anthracene,” *Spectrochimica Acta Part A-molecular and Biomolecular Spectroscopy* **A 29**, 395–403 (1973).
- [35] A. Bree and R. Zwarich, “Raman-scattering tensor elements for some A_g -modes of anthracene,” *Journal of Raman Spectroscopy* **18**, 37–45 (1987).
- [36] J. Brandmul and R. Claus, “Intensity measurements of crystal lattice vibrations In anthracene and naphthalene,” *Spectrochimica Acta Part A - Molecular Spectroscopy* **A 25**, 103–110 (1969).
- [37] F. Z. Khelladi, “Davydov splitting in Raman-spectra of anthracene $C_{14}H_{10}$ and $C_{14}D_{10}$ single-crystals,” *Chemical Physics Letters* **34**, 490–496 (1975).

- [38] D. A. Dows, L. Hsu, S. S. Mitra, O. Brafman, M. Hayek, W. B. Daniels, and R. K. Crawford, "Pressure-dependence of lattice frequencies of anthracene and naphthalene," *Chemical Physics Letters* **22**, 595–599 (1973).
- [39] M. Nicol, M. Vernon, and J. T. Woo, "Raman-spectra and defect fluorescence of anthracene and naphthalene crystals at high-pressures and low-temperatures," *Journal of Chemical Physics* **63**, 1992–1999 (1975).
- [40] H. Shinohara, Y. Yamakita, and K. Ohno, "Raman spectra of polycyclic aromatic hydrocarbons. Comparison of calculated Raman intensity distributions with observed spectra for naphthalene, anthracene, pyrene, and perylene," *Journal of Molecular Structure* **442**, 221–234 (1998).
- [41] K. Hummer, P. Puschnig, and C. Ambrosch-Draxl, "Ab initio study of anthracene under high pressure," *Physical Review B* **67**, 184 105 (2003).
- [42] R. C. Dye and C. J. Eckhardt, "A complete set of elastic-constants of crystalline anthracene by Brillouin-scattering," *Journal of Chemical Physics* **90**, 2090–2096 (1989).
- [43] S. Elnahwy, M. E. Hamamsy, A. C. Damask, D. E. Cox, and W. B. Daniels, "Pressure-dependence of lattice-parameters of anthracene up to 5.4 Kbar and a re-evaluation of elastic-constants," *Journal of Chemical Physics* **68**, 1161–1163 (1978).
- [44] Y. Ishihara and I. Nakada, "Energy gap of crystalline anthracene," *Journal of the Physical Society of Japan* **28**, 667–674 (1970).
- [45] J. Sworakow, "Energy gap anthracene - (comment on paper of Ishihara, Y and Nakada, I)," *Journal of the Physical Society of Japan* **29**, 1390 (1970).
- [46] H. Baessler and Killesre.H, "Bandgap-determination from autoionization data in molecular-crystals," *Molecular Crystals and Liquid Crystals* **24**, 21–31 (1973).
- [47] E. Glockner and H. C. Wolf, "Fluorescence spectrum of anthracene crystals," *Zeitschrift Fur Naturforschung Part A - astrophysik Physik Und Physikalische Chemie A* **24**, 943–951 (1969).
- [48] J. Aaviksoo, G. Liidja, and P. Saari, "Luminescence spectra of anthracene-crystals at 0.4 K," *Physica Status Solidi B - Basic Research* **110**, 69–73 (1982).
- [49] S. Arnold and N. Hassan, "Triplet exciton lifetime under pressure in pure anthracene," *Journal of Chemical Physics* **78**, 5606–5611 (1983).

- [50] L. R. Painter, T. S. Riedinger, R. D. Birkhoff, and J. M. Heller, “Optical-properties of polycrystalline anthracene in the 3.2-9.3 eV spectral region,” *Journal of Applied Physics* **51**, 1747–1750 (1980).
- [51] V. I. Ponomarev and G. V. Shilov, “The crystal-structure of anthracene in 300–100 K range,” *Kristallografiya* **28**, 674–677 (1983).
- [52] L. Zhao, B. J. Baer, and E. L. Chronister, “High-pressure Raman study of anthracene,” *Journal of Physical Chemistry A* **103**, 1728–1733 (1999).
- [53] D. M. Adams and T. K. Tan, “Vibrational spectroscopy at high-pressures. 37. Infrared-spectrum of anthracene,” *Journal of the Chemical Society - Faraday Transactions II* **77**, 1711–1714 (1981).
- [54] P. Schlotter, J. Kalinowski, and H. Bassler, “Photoionization of triplet excitons in tetracene crystals,” *Physica Status Solidi B - Basic Research* **81**, 521–526 (1977).
- [55] P. Petelenz and M. Slawik, “Band-structure of charge-transfer excitons in crystalline tetracene,” *Chemical Physics Letters* **178**, 337–340 (1991).
- [56] M. V. Kurik and Y. P. Piryatinskii, “Luminescence of tetracene crystals,” *Journal of Luminescence* **31-2**, 619–621 (1984).
- [57] G. Vaubel and H. Baessler, “Temperature dependence of width and position of lowest singlet-singlet transition in crystalline tetracene,” *Molecular Crystals and Liquid Crystals* **12**, 39–45 (1970).
- [58] K. Mizuno, A. Matsui, and G. J. Sloan, “Intermediate exciton-phonon coupling in tetracene,” *Journal of the Physical Society of Japan* **53**, 2799–2806 (1984).
- [59] K. Mizuno, A. Matsui, and G. J. Sloan, “Exciton-phonon interaction in tetracene single-crystals under pressure,” *Chemical Physics* **131**, 423–433 (1989).
- [60] C. Goldmann, S. Haas, C. Krellner, K. P. Pernstich, D. J. Gundlach, and B. Batlogg, “Hole mobility in organic single crystals measured by a “flip-crystal” field-effect technique,” *Journal of Applied Physics* **96**, 2080–2086 (2004).
- [61] A. M. Griffiths and P. A. Freedman, “Out-of-plane vibrations of isolated tetracene and pentacene molecules,” *Journal of the Chemical Society - Faraday Transactions II* **78**, 391–398 (1982).

- [62] G. Filippini and C. M. Gramaccioli, “Lattice-dynamical calculations for tetracene and pentacene,” *Chemical Physics Letters* **104**, 50–53 (1984).
- [63] W. F. Maddams and I. A. M. Royaud, “The characterization of polycyclic aromatic-hydrocarbons by Raman-spectroscopy,” *Spectrochimica Acta Part A - Molecular and Biomolecular Spectroscopy* **46**, 309–314 (1990).
- [64] Y. Tomkiewi, R. P. Groff, and P. Avakian, “Spectroscopic approach to energetics of exciton fission and fusion in tetracene crystals,” *Journal of Chemical Physics* **54**, 4504–4507 (1971).
- [65] R. Jankowiak, J. Kalinowski, M. Konys, and J. Buchert, “Solid-state transitions in crystalline tetracene,” *Chemical Physics Letters* **65**, 549–553 (1979).
- [66] M. Rumi, G. Zerbi, K. Mullen, G. Muller, and M. Rehahn, “Nonlinear optical and vibrational properties of conjugated polyaromatic molecules,” *Journal of Chemical Physics* **106**, 24–34 (1997).
- [67] E. Venuti, R. G. Della Valle, L. Farina, A. Brillante, M. Masino, and A. Girlando, “Phonons and structures of tetracene polymorphs at low temperature and high pressure,” *Physical Review B* **70**, 104 106 (2004).
- [68] U. Sondermann, A. Kutoglu, and H. Bassler, “X-ray-diffraction study of the phase-transition in crystalline tetracene,” *Journal of Physical Chemistry* **89**, 1735–1741 (1985).
- [69] K. Kim, Y. K. Yoon, M. O. Mun, S. P. Park, S. S. Kim, S. Im, and J. H. Kim, “Optical properties of solid pentacene,” *Journal of Superconductivity* **15**, 595–598 (2002).
- [70] S. P. Park, S. S. Kim, J. H. Kim, C. N. Whang, and S. Im, “Optical and luminescence characteristics of thermally evaporated pentacene films on Si,” *Applied Physics Letters* **80**, 2872–2874 (2002).
- [71] V. Y. Butko, X. Chi, D. V. Lang, and A. P. Ramirez, “Field-effect transistor on pentacene single crystal,” *Applied Physics Letters* **83**, 4773–4775 (2003).
- [72] K. O. Lee and T. T. Gan, “Space-charge-limited currents in evaporated-films of pentacene,” *Physica Status Solidi A - Applied Research* **43**, 565–571 (1977).
- [73] C. Pannemann, T. Diekmann, and U. Hilleringmann, “Degradation of organic field-effect transistors made of pentacene,” *Journal of Materials Research* **19**, 1999–2002 (2004).

- [74] V. D. Zhukov, M. V. Kurik, Y. P. Piryatinskii, and L. I. Tsikora, “Exciton reflection spectra of pentacene single-crystals at low-temperatures,” *Fizika Tverdogo Tela* **26**, 601–603 (1984).
- [75] T. Aoki-Matsumoto, K. Furuta, T. Yamada, H. Moriya, K. Mizuno, and A. H. Matsui, “Excitonic photoluminescence in pentacene single crystal,” *International Journal of Modern Physics B* **15**, 3753–3756 (2001).
- [76] R. He, I. Dujovne, L. W. Chen, Q. Miao, C. F. Hirjibehedin, A. Pinczuk, C. Nuckolls, C. Kloc, and A. Ron, “Resonant Raman scattering in nanoscale pentacene films,” *Applied Physics Letters* **84**, 987–989 (2004).
- [77] H. Yoshida and N. Sato, “Crystallographic and electronic structures of three different polymorphs of pentacene,” *Physical Review B* **77**, 235 205 (2008).
- [78] A. Brillante, R. G. Della Valle, L. Farina, A. Girlando, M. Masino, and E. Venuti, “Raman phonon spectra of pentacene polymorphs,” *Chemical Physics Letters* **357**, 32–36 (2002).
- [79] C. C. Mattheus, A. B. Dros, J. Baas, A. Meetsma, J. L. de Boer, and T. T. M. Palstra, “Polymorphism in pentacene,” *Acta Crystallographica Section C - Crystal Structure Communications* **57**, 939–941 (2001).
- [80] J. R. Lakowicz, *Principles of Fluorescence Spectroscopy* (Springer, New York, 2006).
- [81] R. E. Sioda, “Electrolytic oxidation of 9,10-diphenylanthracene and properties of its free radical cation and anion,” *Journal of Physical Chemistry* **72**, 2322–2330 (1968).
- [82] M. Yamanuki, M. Oyama, and S. Okazaki, “Resonance Raman measurement of anthracene derivative cation and anion radicals using a column-electrolytic continuous-flow method,” *Vibrational Spectroscopy* **13**, 205–212 (1997).
- [83] A. K. Tripathi, M. Heinrich, T. Siegrist, and J. Pflaum, “Growth and electronic transport in 9,10-diphenylanthracene single crystals - An organic semiconductor of high electron and hole mobility,” *Advanced Materials* **19**, 2097–2101 (2007).
- [84] F. Li, J. L. Lin, J. Feng, G. Chen, H. Y. Liu, S. Y. Liu, L. G. Zhang, X. F. Zhang, and S. T. Lee, “Electrical and optical characteristics of red organic light-emitting diodes doped with two guest dyes,” *Synthetic Metals* **139**, 341–346 (2003).

- [85] X. D. Wang, Y. Sakuratani, H. Sone, K. Tanaka, S. Miyata, and H. Usui, “A diaminomaleonitrile derivative as a new dopant for red-light-emitting electroluminescent device,” *Journal of Physics D-applied Physics* **36**, 1789–1793 (2003).
- [86] D. E. Henn, W. G. Williams, and D. J. Gibbons, “Crystallographic data for an orthorhombic form of rubrene,” *Journal of Applied Crystallography* **4**, 256 (1971).
- [87] M. Saleh, “Transit-time measurements of photogenerated charge-carriers in orthorhombic rubrene crystals,” *Physica Scripta* **21**, 220–222 (1980).
- [88] M. Uchida, C. Adachi, T. Koyama, and Y. Taniguchi, “Charge carrier trapping effect by luminescent dopant molecules in single-layer organic light emitting diodes,” *Journal of Applied Physics* **86**, 1680–1687 (1999).
- [89] E. Botzung-Appert, V. Monnier, T. Ha Duong, R. Pansu, and A. Ibanez, “Polyaromatic luminescent nanocrystals for chemical and biological sensors,” *Chemistry of Materials* **16**, 1609–1611 (2004).
- [90] G. Sakamoto, C. Adachi, T. Koyama, Y. Taniguchi, C. D. Merritt, H. Murata, and Z. H. Kafafi, “Significant improvement of device durability in organic light-emitting diodes by doping both hole transport and emitter layers with rubrene molecules,” *Applied Physics Letters* **75**, 766–768 (1999).
- [91] Y. Hamada, H. Kanno, T. Sano, H. Fujii, Y. Nishio, H. Takahashi, T. Usuki, and K. Shibata, “Organic light-emitting diodes using a gallium complex,” *Applied Physics Letters* **72**, 1939–1941 (1998).
- [92] V. Podzorov, E. Menard, A. Borissov, V. Kiryukhin, J. A. Rogers, and M. E. Gershenson, “Intrinsic charge transport on the surface of organic semiconductors,” *Physical Review Letters* **93**, 086 602 (2004).
- [93] E. Menard, V. Podzorov, S. H. Hur, A. Gaur, M. E. Gershenson, and J. A. Rogers, “High-performance n- and p-type single-crystal organic transistors with free-space gate dielectrics,” *Advanced Materials* **16**, 2097–2101 (2004).
- [94] J. Takeya, M. Yamagishi, Y. Tominari, R. Hirahara, Y. Nakazawa, T. Nishikawa, T. Kawase, T. Shimoda, and S. Ogawa, “Very high-mobility organic single-crystal transistors with in-crystal conduction channels,” *Applied Physics Letters* **90**, 102 120 (2007).
- [95] S. Ono, K. Miwa, S. Seki, and J. Takeya, “A comparative study of organic single-crystal transistors gated with various ionic-liquid electrolytes,” *Applied Physics Letters* **94**, 063 301 (2009).

- [96] J. Takeya, J. Kato, K. Hara, M. Yamagishi, R. Hirahara, K. Yamada, Y. Nakazawa, S. Ikehata, K. Tsukagoshi, Y. Aoyagi, T. Takenobu, and Y. Iwasa, “In-crystal and surface charge transport of electric-field-induced carriers in organic single-crystal semiconductors,” *Physical Review Letters* **98**, 196 804 (2007).
- [97] O. D. Jurchescu, J. Baas, and T. T. M. Palstra, “Effect of impurities on the mobility of single crystal pentacene,” *Applied Physics Letters* **84**, 3061–3063 (2004).
- [98] T. Siegrist, C. Kloc, J. H. Schn, B. Batlogg, R. C. Haddon, S. Berg, and G. A. Thomas, “Enhanced physical properties in a pentacene polymorph,” *Angewandte Chemie - International Edition* **40**, 1732–1736 (2001).
- [99] O. D. Jurchescu, A. Meetsma, and T. T. M. Palstra, “Low-temperature structure of rubrene single crystals grown by vapor transport,” *Acta Crystallographica Section B - Structural Science* **62**, 330–334 (2006).
- [100] E. Venuti, I. Bilotti, R. G. Della Valle, A. Brillante, P. Ranzieri, M. Masino, and A. Girlando, “Polarized Raman spectra of a rubrene single crystal,” *Journal of Physical Chemistry C* **112**, 17 416–17 422 (2008).
- [101] Z. Q. Li, V. Podzorov, N. Sai, M. C. Martin, M. E. Gershenson, M. Di Ventra, and D. N. Basov, “Light quasiparticles dominate electronic transport in molecular crystal field-effect transistors,” *Physical Review Letters* **99**, 016 403 (2007).
- [102] M. Kaschke, N. P. Ernsting, and F. P. Schafer, “Rubrene, a saturable absorber for 308 nm,” *Optics Communications* **66**, 211–215 (1988).
- [103] K. H. Choi, D. H. Hwang, H. M. Lee, L. M. Do, and T. Zyung, “Electroluminescent behaviours of polymer/organic heterostructure devices,” *Synthetic Metals* **96**, 123–126 (1998).
- [104] Z. L. Zhang, X. Y. Jiang, S. H. Xu, T. Nagatomo, and O. Omoto, “The effect of rubrene as a dopant on the efficiency and stability of organic thin film electroluminescent devices,” *Journal of Physics D - Applied Physics* **31**, 32–35 (1998).
- [105] J. Weinberg-Wolf, *Optical Characterization of Organic Semiconducting Single Crystals*, Ph.D. thesis, University of North Carolina at Chapel Hill (2006).
- [106] T. L. Gustafson and F. E. Lytle, “Time-resolved rejection of fluorescence

- from Raman-spectra via high repetition rate gated photon-counting,” *Analytical Chemistry* **54**, 634–637 (1982).
- [107] J. M. Harris, R. W. Chrisman, F. E. Lytle, and R. S. Tobias, “Sub-nanosecond time-resolved rejection of fluorescence from Raman-spectra,” *Analytical Chemistry* **48**, 1937–1943 (1976).
 - [108] S. F. Parker, K. P. J. Williams, P. J. Hendra, and A. J. Turner, “Fourier-transform Raman-spectroscopy using a bench-top FT-IR spectrometer,” *Applied Spectroscopy* **42**, 796–800 (1988).
 - [109] J. R. Weinberg-Wolf, L. E. McNeil, S. Liu, and C. Kloc, “Evidence of low intermolecular coupling in rubrene single crystals by Raman scattering,” *Journal of Physics: Condensed Matter* **19**, 276 204 (2007).
 - [110] B. A. West, J. M. Womick, L. E. McNeil, K. J. Tan, and A. M. Moran, “Ultrafast Dynamics of Frenkel Excitons in Tetracene and Rubrene Single Crystals,” *Journal of Physical Chemistry C* **114**, 10 580–10 591 (2010).
 - [111] R. A. Laudise, C. Kloc, P. G. Simpkins, and T. Siegrist, “Physical vapor growth of organic semiconductors,” *Journal of Crystal Growth* **187**, 449–454 (1998).
 - [112] R. Zeis, C. Besnard, T. Siegrist, C. Schlockermann, X. L. Chi, and C. Kloc, “Field effect studies on rubrene and impurities of rubrene,” *Chemistry of Materials* **18**, 244–248 (2006).
 - [113] P. A. Fleury, S. P. S. Porto, L. E. Cheesman, and H. J. Guggenheim, “Light scattering by spin waves in FeF_2 ,” *Physical Review Letters* **17**, 84–87 (1966).
 - [114] U. Balucani and V. Tognetti, “Light-scattering in Heisenberg antiferromagnets,” *Rivista Del Nuovo Cimento* **6**, 39–104 (1976).
 - [115] J. T. Hougen and S. Singh, “Electronic Raman effect in Pr^{3+} ions in single crystals of PrCl_3 ,” *Physical Review Letters* **10**, 406 (1963).
 - [116] J. T. Hougen and S. Singh, “Electronic and vibrational Raman spectra of PrCl_3 and LaCl_3 ,” *Proceedings of the Royal Society of London. Series A, Mathematical and Physical Sciences* **277**, 193 (1964).
 - [117] W. Hayes and R. Loudon, *Scattering of Light by Crystals* (Wiley, New York, 1978).
 - [118] P. Y. Yu and M. Cardona, *Fundamentals of Semiconductors: Physics and Materials Properties* (Springer, New York, 1995).

- [119] O. Mitrofanov, D. V. Lang, C. Kloc, J. M. Wikberg, T. Siegrist, W. Y. So, M. A. Sergent, and A. P. Ramirez, “Oxygen-related band gap state in single crystal rubrene,” *Physical Review Letters* **97**, 166 601 (2006).
- [120] L. B. Humphreys, “Ionic Raman effect. III. first- and second-order ionic Raman effects,” *Physical Review B* **6**, 3886–3897 (1972).
- [121] R. A. Cowley, “Theory of Raman scattering from crystals,” *Proceedings of the Physical Society of London* **84**, 281–296 (1964).
- [122] R. A. Cowley, “Anharmonic crystals,” *Reports On Progress In Physics* **31**, 123–166 (1968).
- [123] P. G. Klemens, “Anharmonic decay of optical phonons,” *Physical Review* **148**, 845–848 (1966).
- [124] S. Safran and B. Lax, “Temperature-dependence of Raman linewidth and frequency-shift In Ge and Si,” *Journal of Physics and Chemistry of Solids* **36**, 753–757 (1975).
- [125] J. Menéndez and M. Cardona, “Temperature dependence of the first-order Raman scattering by phonons in Si, Ge, and α -Sn: Anharmonic effects,” *Physical Review B* **29**, 2051–2059 (1984).
- [126] K. Ohno, H. Mutoh, and Y. Harada, “Application of Penning ionization electron spectroscopy to the study of chemical reactions on the solid surface; Photooxidation of naphthacene and rubrene,” *Surface Science* **115**, L128–L132 (1982).
- [127] C. Kloc, K. J. Tan, M. L. Toh, K. K. Zhang, and Y. P. Xu, “Purity of rubrene single crystals,” *Applied Physics A - Materials Science & Processing* **95**, 219–224 (2009).
- [128] P. Hohenberg and W. Kohn, “Inhomogeneous electron gas,” *Physical Review* **136**, B864–B871 (1964).
- [129] J. M. Robertson, “Structure of naphthalene and anthracene,” *Reviews of Modern Physics* **30**, 155–158 (1958).
- [130] V. Langer and H. D. Becker, “Crystal-structure of 9,10-diphenylanthracene, (c6h5)(c14h8)(c6h5),” *Zeitschrift Fur Kristallographie* **199**, 313–315 (1992).
- [131] D. Holmes, S. Kumaraswamy, A. J. Matzger, and K. P. C. Vollhardt, “On the nature of nonplanarity in the [N]phenylenes,” *Chemistry - A European Journal* **5**, 3399–3412 (1999).

- [132] R. G. Endres, C. Y. Fong, L. H. Yang, G. Witte, and C. Woll, “Structural and electronic properties of pentacene molecule and molecular pentacene solid,” *Computational Materials Science* **29**, 362–370 (2004).
- [133] J. M. Adams and S. Ramdas, “Crystal-structure of solution-grown 9,10-diphenylanthracene - combined computational and X-ray study,” *Acta Crystallographica Section B - structural Science* **35**, 679–683 (1979).
- [134] I. Bulgarovskaya, V. M. Vozzhennikov, S. B. Aleksandrov, and V. K. Belsky, *Latv. PSR Zinat. Akad. Vestis, Fiz. Teh. Zinat. Ser.* **4**, 53 (1983).
- [135] Y. Hamada, H. Kanno, T. Tsujioka, H. Takahashi, and T. Usuki, “Red organic light-emitting diodes using an emitting assist dopant,” *Applied Physics Letters* **75**, 1682–1684 (1999).
- [136] D. A. da Silva Filho, E. G. Kim, and J. L. Brédas, “Transport properties in the rubrene crystal: Electronic coupling and vibrational reorganization energy,” *Advanced Materials* **17**, 1072–1076 (2005).
- [137] M. T. Dove, *Introduction to Lattice Dynamics* (Cambridge University Press, New York, 1993).
- [138] R. G. Della Valle, E. Venuti, L. Farina, A. Brillante, M. Masino, and A. Girlando, “Intramolecular and low-frequency intermolecular vibrations of pentacene polymorphs as a function of temperature,” *Journal of Physical Chemistry B* **108**, 1822–1826 (2004).
- [139] O. D. Jurchescu, *Molecular Organic Semiconductors for Electronic Devices*, Ph.D. thesis, University of Groningen (2006).
- [140] Z. Q. Ren, L. E. McNeil, S. B. Liu, and C. Kloc, “Molecular motion and mobility in an organic single crystal: Raman study and model,” *Physical Review B* **80**, 245 211 (2009).
- [141] R. Loudon, “The Raman effect in crystals,” *Advances In Physics* **50**, 813–864 (2001).
- [142] M. J. Frisch, G. W. Trucks, H. B. Schlegel, G. E. Scuseria, M. A. Robb, J. R. Cheeseman, J. A. Montgomery, Jr., T. Vreven, K. N. Kudin, J. C. Burant, J. M. Millam, S. S. Iyengar, J. Tomasi, V. Barone, B. Mennucci, M. Cossi, G. Scalmani, N. Rega, G. A. Petersson, H. Nakatsuji, M. Hada, M. Ehara, K. Toyota, R. Fukuda, J. Hasegawa, M. Ishida, T. Nakajima, Y. Honda, O. Kitao, H. Nakai, M. Klene, X. Li, J. E. Knox, H. P. Hratchian, J. B. Cross, V. Bakken, C. Adamo, J. Jaramillo, R. Gomperts, R. E. Stratmann, O. Yazyev, A. J. Austin, R. Cammi, C. Pomelli, J. W. Ochterski,

- P. Y. Ayala, K. Morokuma, G. A. Voth, P. Salvador, J. J. Dannenberg, V. G. Zakrzewski, S. Dapprich, A. D. Daniels, M. C. Strain, O. Farkas, D. K. Malick, A. D. Rabuck, K. Raghavachari, J. B. Foresman, J. V. Ortiz, Q. Cui, A. G. Baboul, S. Clifford, J. Cioslowski, B. B. Stefanov, G. Liu, A. Liashenko, P. Piskorz, I. Komaromi, R. L. Martin, D. J. Fox, T. Keith, M. A. Al-Laham, C. Y. Peng, A. Nanayakkara, M. Challacombe, P. M. W. Gill, B. Johnson, W. Chen, M. W. Wong, C. Gonzalez, and J. A. Pople, "Gaussian 03, Revision C.02," Gaussian, Inc., Wallingford, CT, 2004.
- [143] R. G. Parr and W. Yang, *Density-Functional Theory of Atoms and Molecules* (Oxford University Press, Oxford, U.K., 1989).
- [144] A. D. Becke, "Density-functional exchange-energy approximation with correct asymptotic behavior," *Physical Review A* **38**, 3098–3100 (1988).
- [145] A. D. Becke, "Density-functional thermochemistry. III. The role of exact exchange," *Journal of Chemical Physics* **98**, 5648–5652 (1993).
- [146] C. Lee, W. Yang, and R. G. Parr, "Development of the Colle-Salvetti correlation-energy formula into a functional of the electron density," *Physical Review B* **37**, 785–789 (1988).
- [147] R. Krishnan, J. S. Binkley, R. Seeger, and J. A. Pople, "Self-consistent molecular orbital methods XX. A basis set for correlated wave functions," *Journal of Chemical Physics* **72**, 650–654 (1980).
- [148] M. J. Frisch, J. A. Pople, and J. S. Binkley, "Self-consistent molecular orbital methods 25. Supplementary functions for Gaussian basis sets," *Journal of Chemical Physics* **80**, 3265–3269 (1984).
- [149] R. A. Marcus, "On the theory of oxidation-reduction reactions involving electron transfer. I," *Journal of Chemical Physics* **24**, 966–978 (1956).
- [150] R. A. Marcus, "Electron transfer reactions in chemistry. Theory and experiment," *Reviews of Modern Physics* **65**, 599–610 (1993).
- [151] W. Q. Deng and W. A. Goddard, "Predictions of hole mobilities in oligoacene organic semiconductors from quantum mechanical calculations," *Journal of Physical Chemistry B* **108**, 8614–8621 (2004).
- [152] S. Mohakud and S. K. Pati, "Large carrier mobilities in octathio[8]circulene crystals: a theoretical study," *Journal of Materials Chemistry* **19**, 4356–4361 (2009).
- [153] K.-C. Kao and W. Hwang, *Electrical Transport in Solids*, Vol. 14 (Pergamon, New York, 1981).

- [154] W. Y. So, J. M. Wikberg, D. V. Lang, O. Mitrofanov, C. L. Kloc, T. Siegrist, A. M. Sergent, and A. P. Ramirez, “Mobility-independent doping in crystalline rubrene field-effect transistors,” *Solid State Communications* **142**, 483–486 (2007).
- [155] C. Krellner, S. Haas, C. Goldmann, K. P. Pernstich, D. J. Gundlach, and B. Batlogg, “Density of bulk trap states in organic semiconductor crystals: Discrete levels induced by oxygen in rubrene,” *Physical Review B* **75**, 245 115 (2007).
- [156] O. Mitrofanov, C. Kloc, T. Siegrist, D. V. Lang, W. Y. So, and A. P. Ramirez, “Role of synthesis for oxygen defect incorporation in crystalline rubrene,” *Applied Physics Letters* **91**, 212 106 (2007).
- [157] G. Schuck, S. Haas, A. F. Stassen, H. J. Kirner, and B. Batlogg, “5,12-Bis(4-*tert*-butylphenyl)-6,11-diphenylnaphthacene,” *Acta Crystallographica Section E - Structure Reports Online* **63**, o2893 (2007).
- [158] S. Haas, A. F. Stassen, G. Schuck, K. P. Pernstich, D. J. Gundlach, B. Batlogg, U. Berens, and H. J. Kirner, “High charge-carrier mobility and low trap density in a rubrene derivative,” *Physical Review B* **76**, 115 203 (2007).